DEPARTMENT OF PHYSICS
UNIVERSITY OF JYVÄSKYLÄ
RESEARCH REPORT No. 6/2012

DEVELOPMENT OF NIOBIUM-BASED SUPERCONDUCTING JUNCTIONS

BY
MINNA NEVALA

Academic Dissertation
for the Degree of
Doctor of Philosophy

To be presented, by permission of the
Faculty of Mathematics and Science
of the University of Jyväskylä,
for public examination in Auditorium FYS-1 of the
University of Jyväskylä on August 1, 2012
at 12 o'clock noon

Jyväskylä, Finland
August, 2012

Preface

The work presented in this thesis has been carried out during the years 2004-2012 at the Department of Physics and Nanoscience Center in the University of Jyväskylä.

First of all, I would like to thank my supervisor Prof. Ilari Maasilta for the guidance and giving me the opportunity to work in his inspiring group and in this interesting field of nanophysics. It has been a privilege to collaborate and work with many brilliant and great people during these years.

I wish to express my warmest gratitude to Dr. Saumyadip Chaudhuri for a very fruitful collaboration and the linguistic review. The collaboration with Dr. Jenni Karvonen and Mr. Jaakko Halkosaari is gratefully acknowledged. In addition, I wish to thank Dr. K. Senapati and Prof. R. C. Budhani from Indian Institute of Technology, Mr. T. Hakkarainen and Prof. T. Niemi from Tampere University of Technology, Dr. V. V. Yurchenko, Prof. T. H. Johansen and his research group from University of Oslo for collaboration.

I am grateful to all the present members of our group, who are not yet mentioned. Particularly, I wish to thank Mr. Zhuoran Geng, Mr. Tero Isotalo, Mr. Juhani Julin, Dr. Kimmo Kinnunen, Mr. Mikko Palosaari, Dr. Tuomas Puurtinen, Ms. Yaolan Tian and Mr. Andrii Torgovkin. It has been a pleasure to work with you.

Many thanks go to all the former members of our group, all the people from Nanoscience Center and the Department of Physics for pleasant working environment and fascinating discussions. Especially, I wish to thank Dr. Jenni Andersin, Ms. Khattiya Chalapat, Dr. Panu Koppinen, Dr. Thomas Kühn, Dr. Lasse Taskinen and Dr. Nobuyuki Zen. Technical support from the laboratory engineers Mr. Antti Nuottajärvi and Mr. Tarmo Suppula has been essential and is gratefully acknowledged.

Financial support from Finnish Foundation for Technology Promotion, Ulla Tuominen Foundation and the Academy of Finland are gratefully acknowledged.

Finally, I would like to thank my relatives and friends for the encouragement and support. I owe my deepest gratitude to my love, Juha.

Jyväskylä, August 2012

Minna Nevala

Abstract

Nevala, Minna
Development of niobium-based superconducting junctions
Jyväskylä: University of Jyväskylä, 2012
(Research report/Department of Physics, University of Jyväskylä,
ISSN 0075-465X; 6/2012)
ISBN 978-951-39-4789-7
diss.

This thesis presents a review of publications which mainly focuses on the fabrication and performance of Nb-based normal metal-insulator-superconductor (NIS) tunnel junctions and superconductor-normal metal-superconductor (SNS) Josephson junctions at low temperatures.

The Cu/AlO_x-Al/Nb based NIS double tunnel junctions were successfully fabricated using conventional electron beam lithography combined with multi-angle thermal evaporation of metals in ultra high vacuum. The subgap characteristics of these junctions showed expected temperature dependence from 0.2 K to 5 K with a good thermometry sensitivity 0.2-0.3 mV/K. Signatures of small electronic cooling effects were observed near the Nb superconducting gap edge.

Thin films of NbN were successfully deposited on (100)-oriented MgO using laser pulses from excimer and Nd:YAG lasers. The NbN films deposited using the 1064 nm laser pulses from Nd:YAG laser were studied further. An excellent quality of the NbN films was reflected as smooth surfaces of the films and critical temperature (T_C) as high as $\sim$16 K. A strong correlation between T_C, the lattice parameter of deposited NbN and ambient nitrogen gas pressure during the film ablation was observed. In addition, thin films of NbN were successfully employed in studies of suppression of superconductivity in the influence of an applied magnetic field.

Pulsed laser deposited NbN films were used to fabricate Cu/AlO_x-Al/NbN based NIS tunnel junction devices where the fabrication included an overlay electron beam lithography and multi-angle evaporation of Al and Cu layers. The subgap conductance of these junctions also showed appreciable dependence on the temperature. The broadening of the density of the states of the NbN was found small enough for potential cooling applications, but the native niobium oxide on the sur-

face of NbN gave a high value of the tunneling resistance, which would limit the cooling power of the devices.

Trilayers of pulsed laser deposited NbN/TaN/NbN were fabricated into SNS based Josephson junctions, using an unconventional method with electron-beam lithography and lift-off of chemical vapor deposited insulating layers. The quality of the junctions was tested by investigating the temperature dependence of the product of the critical current and normal state resistance. The obtained values are of the same order of magnitude as previous studies and are high enough values for practical applications.

Keywords Pulsed laser deposition, thin films, superconducting device fabrication, NIS tunnel junctions, SNS Josephson junctions

Author's address Minna Nevala
Department of Physics
Nanoscience Center
University of Jyväskylä
Finland

Supervisor Professor Ilari Maasilta
Department of Physics
Nanoscience Center
University of Jyväskylä
Finland

Reviewers Professor Petriina Paturi
Department of Physics and Astronomy
University of Turku
Finland

Dr. David Gunnarsson
Technical Research Centre of Finland
VTT
Finland

Opponent Dr. Masataka Ohkubo
The National Institute of Advanced Industrial Science and Technology
AIST
Tsukuba
Japan

List of Publications

The main results of this thesis have been reported in the following articles:

A.I. M. R. NEVALA, I. J. MAASILTA, K. SENAPATI AND R. C. BUDHANI, *Fabrication and Characterization of Epitaxial NbN/TaN/NbN Josephson Junctions Grown by Pulsed Laser Ablation*. IEEE Trans. Appl. Supercond. **19** (2009) 253 -256.

A.II. S. CHAUDHURI, M. R. NEVALA, T. HAKKARAINEN, T. NIEMI AND I. J. MAASILTA, *Infrared Pulsed Laser Deposition of Niobium Nitride Thin Films*. IEEE Trans. Appl. Supercond. **21** (2011) 143 -146.

A.III. M. R. NEVALA, S. CHAUDHURI AND I. J. MAASILTA, *Fabrication and conductance characteristics of niobium nitride based superconducting tunnel junctions*. Submitted for publication.

A.IV. M. R. NEVALA, S. CHAUDHURI, J. HALKOSAARI. J. T. KARVONEN AND I. J. MAASILTA, *Sub-micron normal-metal/insulator/superconductor tunnel junction thermometer and cooler using Nb*. Submitted for publication.

A.V. V. V. YURCHENKO, D. V. SHANTSEV, T. H. JOHANSEN, M. R. NEVALA, I. J. MAASILTA, K. SENAPATI AND R. C. BUDHANI, *Reentrant stability of superconducting films and the vanishing of dendritic flux instability*. Phys. Rev. B **76** (2007) 092504.

A.VI. A. J. QVILLER, V. V. YURCHENKO, K. ELIASSEN, J. I. VESTGÅRDEN, T. H. JOHANSEN, M. R. NEVALA, I. J. MAASILTA, K. SENAPATI AND R. C. BUDHANI, *Irreversibility of the threshold field for dendritic flux avalanches in superconductors*. Physica C: Superconductivity **470** (2010) 897-900.

Author's contribution

The author of this thesis has written the first drafts of the articles A.I, A.III and A.IV and participated in writing the first draft of the article A.II. The author has fabricated all the samples in A.I-A.VI, excluding the pulsed laser deposition and the sample 15 (30) nm in A.IV. The measurements and data analysis was fully done by the author in A.I, and partly in A.III and A.IV. The $I - V$ measurements in A.II were done by the author.

Other publications to which the author has contributed

B.I. J. PENTTILÄ, A. VIRTANEN, M. NEVALA, K. KINNUNEN, A. LUUKANEN, J. HASSEL, M. KIVIRANTA, P. HELISTÖ, I. MAASILTA AND H. SEPPÄ , *Development of SQUID amplifier and ac-biased bolometer for detection of sub-mm radiation*. URSI/IEEE XXIX Convention on Radio Science, ed. Manu Lahdes, VTT Symposium 235, pp. 139-142, Espoo (2004).

B.II. P. LAITINEN, M. NEVALA, A. PIROJENKO, K. RANTTILA, R. SEPPÄLÄ, I. RIIHIMÄKI, J. R.ÄISÄNEN B AND A. VIRTANEN, *Utilisation of a sputtering device for targetry and diffusion studies*. Nuclear Instruments and Methods in Physics Research Section B: Beam Interactions with Materials and Atoms **226** (2004) 441-446.

Contents

Preface **i**

Abstract **iii**

List of Publications **vii**

1 Introduction **1**

2 Theoretical aspects **5**
2.1 General description of tunnel junctions 5
2.2 Description of tunneling currents 7
2.3 Josephson junctions 10
2.3.1 Josephson junctions with RCSJ model 11
2.3.2 Josephson junctions with RSJ model 13
2.3.3 The proximity effect and Andreev reflection 14
2.3.4 Likharev's theory for critical current of SNS junctions 15
2.3.5 Josephson junctions under the influence of magnetic field . . 15
2.3.6 Rapid single flux quantum logic 17
2.4 Applications of the NIS junctions: thermometry and cooling 17
2.4.1 NIS junctions as thermometers 18
2.4.2 NIS junctions as coolers 19

3 Experimental techniques and theory of thin film growth **23**
3.1 Pulsed laser deposition 23
3.1.1 Thermal cycle 24
3.1.2 Nd:YAG and excimer lasers 25
3.1.3 Drawbacks of PLD 26
3.2 Thin film growth 27
3.3 Thin film deposition with UHV and PECVD systems 30
3.3.1 Electron beam lithography 31
3.3.2 Plasma cleaning and reactive ion etching 32
3.3.3 Sputtering 32
3.3.4 Measurements at low temperatures 32

4 Pulsed laser deposition of niobium nitride thin films and device fabrication **35**
4.1 Nitrides of niobium and tantalum 35
4.1.1 Nitrides of niobium 35

4.1.2 Oxides of NbN 37
4.1.3 TaN 37
4.2 Pulsed laser deposition and properties of NbN 37
4.2.1 The fabrication details of Cu/AlO_x-Al/NbN and Cu/NbO_x/NbN based tunnel junctions 40
4.2.2 Fabrication of SNS Josephson junctions 42
4.2.3 Fabrication of NbN samples for magneto-optical imaging . . 44
4.2.4 Fabrication of Cu/AlO_x-Al/Nb based tunnel junctions 45

5 Experimental results **47**
5.1 Performance of the Cu/AlO_x-Al/Nb based tunnel junctions 47
5.2 Performance of the Cu/AlO_x-Al/NbN based tunnel junctions 51
5.2.1 Performance of $NbN/NbO_x/Cu/NbO_x$/NbN junction at 4.2 K 54
5.3 Performance of the SNS Josephson junctions 56

6 Conclusions **63**

Chapter 1

Introduction

Superconductivity, an interesting phenomena that defies logic and common sense, was discovered a hundred and one years ago by H. Onnes and colleagues [1]. The research group had previously liquefied helium (^{4}He), which gave them the necessary tools to reach a temperature of few degrees above absolute zero. An era of cryogenic experiments followed. In 1960's after the invention of a continuously operating dilution refrigerator with ^{3}He$-^4$He mixture, refrigeration below 1 K became easier and a routine process [1]. The breakthrough describing superconductivity in a microscopic level, taking quantum mechanical theory into account, was presented in 1950's by Bardeen, Cooper and Schrieffer [2]. Till date, a large number of different superconducting metals and compounds have been discovered with transition temperatures ranging from a few millikelvins to that of liquid nitrogen and above [3]. For small scale electronic devices thin metallic films are mainly used as superconductors, owing to their great reliability and ease of fabrication.

A very thin insulating (I) layer separating a normal metal (N) and a superconductor (S) constitutes a NIS tunnel junction. These NIS junction based devices are promising for reliable low temperature thermometry applications [4], micrometer scale solid state coolers [5–7], and ideal single electron transistors [8]. The temperature range for thermometry for such devices depends upon the transition temperature (T_C) of the superconductor, while the maximum cooling power is proportional to the square of the superconducting gap (Δ). This translates to large cooling power for intermediate T_C based NIS devices, at least at low temperatures where the electron-phonon coupling is weak.

Typically, aluminium (Al) has dominated the choice as the superconductor in NIS based devices, since it can be easily evaporated and then oxidized to form AlO_x with excellent insulating properties. The drawbacks of using an Al thin film is its low $T_C \sim 1.5$ K and hence a small $\Delta_{Al} \sim 0.23$ meV [4]. A straightforward idea to achieve higher cooling power and larger thermometry range is to use niobium (Nb)

with $T_C \sim 9$ K and $\Delta_{\mathrm{Nb}} \sim 1.5$ meV [9,10] as the superconductor.

For microbolometers, when a superconductor with T_C higher than liquid ^{4}He temperature (4.2 K) is needed, niobium has traditionally been the primary choice. A superconducting antenna-coupled Nb-microbolometer consists of a micrometer size thermal sensing element and a logarithmic spiral antenna, presented in Fig. 1.1. Thermal isolation of the sensing element from substrate is achieved using a vacuum-bridge geometry [11]. The fraction of the normal region in the sensing element depends upon the incident radiation flux as a consequence of which the current through the bridge changes under constant voltage. Large arrays of Nb-bolometer detectors can be fabricated with lithographic techniques, which makes Nb-microbolometers a promising candidate for concealed weapon detection in the submillimeter radiation range [12].

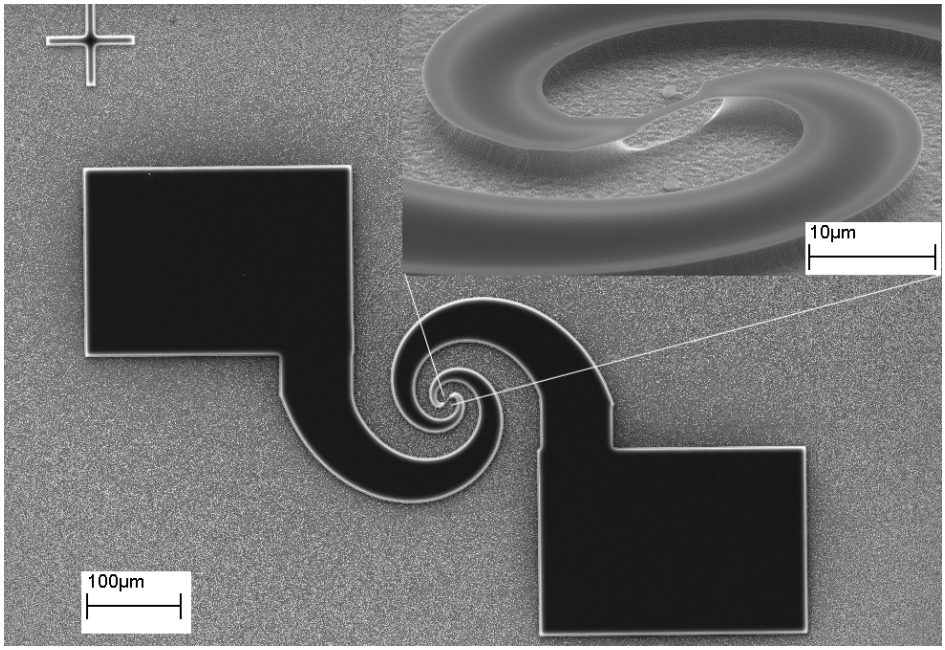

FIGURE 1.1 A scanning electron micrograph of an antenna-coupled Nb-microbolometer fabricated at NSC Jyväskylä by the author. The inset shows a tilt angle view of the thermally isolated vacuum-bridge. Figure adapted from Ref. [B.I].

However, the major drawback of Nb for superconductor-insulator-superconductor (SIS) based Josephson junction device fabrication is in difficulty of its oxidation [13]. The oxide layer on the Nb surface comprises of several different suboxides [14], which exhibit various phases: insulating, metallic and even superconducting. These various oxide phases are segregated and serrated on the surface. This very nature of uneven oxidation leads to unstable device characteristics. However, this problem can be surmounted by covering the Nb electrode with a very thin

layer of Al *in situ*, and then oxidizing the latter during the process of device fabrication [15,16]. Nevertheless, there have been suggestions that evaporated Nb might not be an ideal material for electronic cooler devices, because of a large broadening of the subgap superconducting density of states [10] and other fabrication related difficulties.

Traditionally Nb/AlO_x/Nb junctions are deposited *in situ* first as trilayers and after that the junctions are fabricated *ex situ*. Such *ex situ* processes are fairly complex and include coating and etching, thereby making the fabrication of a submicrometer scale junction a difficult task. One reason why this trilayer process is used is to avoid the usage of polymer resists during deposition. Such polymer resists are widely used for micrometer scale device fabrication, however, such resists tend to degas and decompose which can contaminate the superconductor material and thus suppress the T_C [13,17,18]. The use of such polymer based resist layers have given contradictory results. Thin Nb lines, submicron scale Nb-based SIS tunnel junctions and Al/AlO_x/Nb-based NIS tunnel junctions (operating above 1.9 K) with high T_C have already been successfully fabricated using conventional resist polymers, e-beam lithography and metal evaporation in UHV system [9,19]. Now Cu/AlO_x-Al/Nb based NIS junctions have been shown to possess a good thermometry sensitivity from 0.2 K to 5 K and some cooling [A.IV]. The crucial features for the deposition of high quality Nb with resist polymers are high base vacuum, a large substrate to Nb crucible distance [9,19] and more thermally stable resist polymer [20].

Another potential Nb based material, namely nitride of niobium (NbN), has shown promising properties in terms of Δ and T_C, especially in the rocksalt and simple cubic structures with T_C as high as $\sim$16-17.3 K and Δ_{NbN} $\sim$2.5-3.0 meV [21–24]. However, compared to Nb, the fabrication of NbN thin film is not so straightforward. The critical temperature of NbN depends strongly on the Nb:N ratio, and even a slight off-stoichiometry leads to a suppression of the transition temperature [A.II]. In addition to giving an intermediate range T_C, NbN is a versatile material with good stability against strain, chemical and mechanical attacks, and it has been used in several applications such as NbN-microbolometers [25], Cu/AlO_x-Al/NbN based tunnel junctions [A.III], and superconductor-normal metal-superconductor (SNS) Josephson junctions [A.I], [26].

NbN/TaN/NbN based SNS Josephson junctions exhibit a non-hysteretic current-voltage curve and they can be therefore directly used as elements of rapid single flux quantum logic, a candidate for high speed electronic devices [27]. The performance of such a SNS device depends strongly on the resistivity of the normal metal. Interestingly, the resistivity of TaN can be tuned during the trilayer deposition, since the TaN properties are sensitive to the Ta:N ratio, similar to NbN.

Apart from being used as a superconducting material for junctions, NbN can be employed for studying fundamental properties of superconductivity, for example the mechanism of the suppression of superconductivity. Figure 1.2 shows magneto-optical images of the unusual penetration pattern of an applied magnetic field into a thin NbN film [A.V, A.VI], [28].

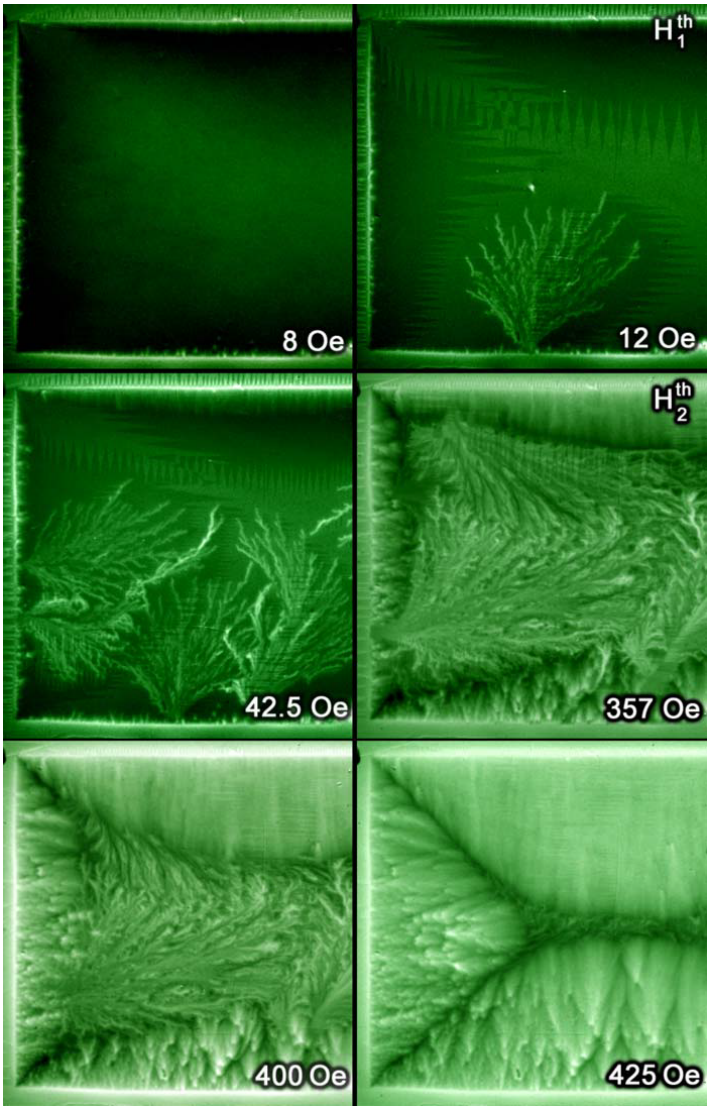

FIGURE 1.2 Magneto-optical images of a superconducting NbN thin film under the influence of an increasing magnetic field. Only the left half of the image is shown. Figure adapted from Ref. [A.V].

Chapter 2

Theoretical aspects

This chapter briefly reviews the basic theoretical aspects of tunnel junctions, in the framework of the Bardeen, Cooper, and Schrieffer (BCS) theory [2]. First a brief description of a tunnel junction is presented, which is followed by the theory of quantum mechanical tunneling of quasiparticles between two electrodes, which can be metallic or superconducting. The idea of tunnel junction thermometry and cooling at low temperatures are also explored. Finally the fundamentals of Josephson junctions are discussed.

2.1 General description of tunnel junctions

A tunnel junction is typically a thin insulating barrier ($\sim$ Ångströms to few nanometers) sandwiched between two electrodes. These electrodes can be either superconducting or normal metal. For a working tunnel junction device the insulating barrier should be thin enough so that quantum mechanical probability for electrons tunneling through the barrier is sufficient.

The thickness and transparency of the tunneling barrier play an important role in defining the rate of tunneling [2,29]. Moreover, the transparency of the insulating barrier should be high enough so that when voltage V is applied across the junction, tunneling is possible with practical rate. Very first NIS tunnel junctions were demonstrated in the 1960's by Giaver [30], who used oxidized aluminium as the barrier material. Aluminium oxide still dominates the choice as the barrier material even today. For practical use, it is beneficial to connect two NIS junctions in series, thereby forming a SINIS structure, a schematic of which is shown in Fig. 2.1.

The microscopic description of superconductivity is given by the BCS theory [2]. According to it, the superconducting energy gap is temperature dependent,

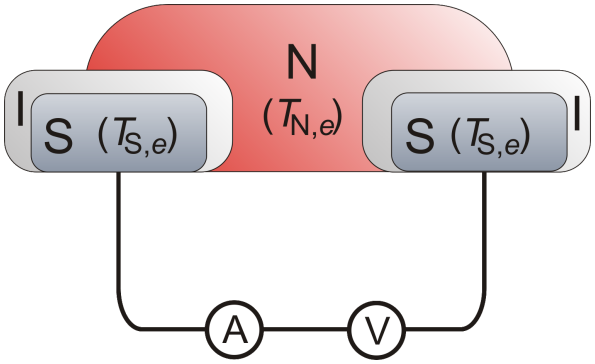

FIGURE 2.1 A schematics of a superconductor-insulator-normal metal double junction SINIS, $T_{\mathrm{N},e}$ is the (electron) temperature of normal metal and $T_{\mathrm{S},e}$ represents the (electron) temperature of superconductor, A and V are the circuit current and voltage respectively. Figure adapted from Ref. [31].

gaining the maximum value at zero temperature [2] and is given by the equation

$$\Delta(0) = 1.764 \times k_B T_C, \tag{2.1}$$

where k_B is the Boltzmann constant.

The critical temperature and thus the superconducting energy gap are material dependent [3]. For metallic elements, the highest values are exhibited by niobium ($\Delta_{\mathrm{Nb}} \sim 1.5$ meV, $T_C \sim 9.2$ K) [32], while typical aluminium thin films have $\Delta_{\mathrm{Al}} \sim 0.22$ meV and $T_C \sim 1.2$ K [4]. However, the value of the superconducting gap can vary even for the same metal, depending on the film quality, impurity content and thickness [5]. For example, the critical temperature of Nb is very sensitive to film deposition conditions [9], while the energy gap of Al can be increased by decreasing the film thickness [33,34]. This however is not a general trend, for example the value of Δ for niobium nitride (NbN) decreases with decreasing film thickness [35, 36]. Moreover, superconducting properties of niobium nitride are very sensitive to other deposition parameters [A.II], [37,38].

The Fermi function $f_i(E, T_i)$ describes the occupancy probability of electron states at energy E with the temperature T_i in the electrode i, and is given by

$$f_i(E, T_i) = \frac{1}{\mathrm{e}^{(E-\mu)/k_B T_i} + 1} \tag{2.2}$$

where μ is the chemical potential. At low temperatures $\mu \approx E_F$, where E_F is the Fermi energy.

At finite temperatures, some electrons in the superconductor are in the two electron bound state (Cooper pairs), while other electrons behave as single quasi-

particles. According to the BCS theory, the density of states in the superconducting state differs from that of normal metal state [2]. Electron states do not exist inside the superconducting gap and the normalized quasiparticle density of states (DOS) is

$$n_{\mathrm{S}}(E,T) = \frac{N_{\mathrm{S}}(E)}{N_{\mathrm{N}}(0)} = \begin{cases} \frac{|E|}{\sqrt{E^2-\Delta(T)^2}}, & |E| > \Delta(T) \\ 0 \qquad\qquad\quad , & |E| < \Delta(T) \end{cases} \tag{2.3}$$

where $N_{\mathrm{S}}(E)$ is quasiparticle density of states of the metal in superconducting state, $N_{\mathrm{N}}(0)$ is density of states in normal metal at fermi energy and E is measured from $E_F = 0$. An assumption that $N_{\mathrm{N}}(0)$ is a constant is made in equation (2.3). At low temperature, it is a good approximation as the thermal energy $k_B T$ is significantly smaller than Fermi energy, $k_B T \ll E_F$ [2, 39].

However, in real experiments the values of $N_{\mathrm{S}}(E)$ deviates from ideal behavior given by equation (2.3). A more appropriate model describing the real DOS includes the so-called Dynes parameter (Γ) [5, 40]. The normalized (Dynes) density of states is given by

$$n_{\mathrm{S}}(E,T) = \left| \mathrm{Re}\left(\frac{E + i\Gamma}{\sqrt{(E+i\Gamma)^2 - (\Delta(T))^2}} \right) \right|. \tag{2.4}$$

As a result of the finite lifetime of quasiparticles, some energy states are created within superconducting gap, and the singularity at the gap-edge disappears [40, 41]. In the limit $\Gamma \to 0$, equation (2.4) approaches equation (2.3). In this work we discovered that Nb has a Dynes parameter $\Gamma'_{\mathrm{Nb}} = \Gamma_{\mathrm{Nb}}/\Delta_{\mathrm{Nb}}(0) \sim 10^{-2}$ while that of Al is often at least two orders of magnitude smaller $\Gamma'_{\mathrm{Al}} = \Gamma_{\mathrm{Al}}/\Delta_{\mathrm{Al}}(0) \sim 2 \times 10^{-4}$ [4], but can be even lower [42]. Apart from the finite lifetime effects, the other explanations of the origin of Γ have been generally attributed to two-particle events (Andreev currents), impurities and pinholes in the tunneling barrier [43, 44].

2.2 Description of tunneling currents

The total tunneling current through a NIS junction is given by [2]

$$I(V,T) = \frac{1}{eR_{\mathcal{T}}} \int_{-\infty}^{\infty} n_{\mathrm{S}}(E)[f_{\mathrm{S}}(E,T) - f_{\mathrm{N}}(E+eV,T)]\mathrm{d}E. \tag{2.5}$$

where n_{S} is superconductor density of states, $R_{\mathcal{T}} = \hbar/(4\pi e^2 \mathcal{A}|\mathcal{T}|^2 N_{\mathrm{N}}(0) N_{\mathrm{S}}(0))$ is the tunneling resistance where $\mathcal{A}$ is the area of the tunnel junction and $\mathcal{T}$ represents tunneling amplitude, and $\hbar$ is the reduced Planck constant [2, 31]. At zero temperature, the differential conductance $\mathrm{d}I/\mathrm{d}V$ gives the density of states [2]. A tunneling event from a normal metal to a superconductor is illustrated in Fig. 2.2.

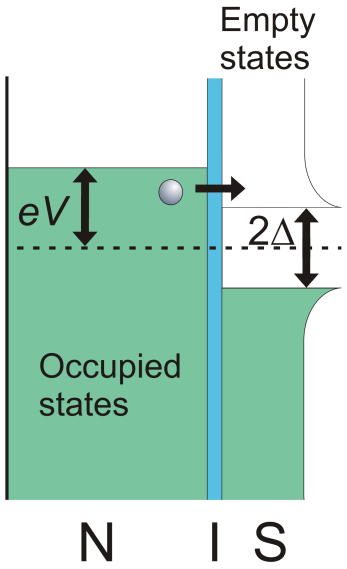

FIGURE 2.2 An occupation diagram showing a tunneling event from normal metal (N) to superconductor (S) at zero temperature under applied bias eV.

With increasing temperature, the gap edge features are smeared in $\mathrm{d}I/\mathrm{d}V$ and the peak at the gap edge progressively reduced [2]. Finally, at temperatures above T_C the superconductor returns to its normal state and, the $I-V$ characteristics are linear, representing normal metal-insulator-normal metal (NIN) tunneling. Theoretical current-voltage ($I-V$) and differential conductance-voltage ($\mathrm{d}I/\mathrm{d}V-V$) characteristics for a NIS junction are presented at figures 2.3(a) and (b).

Two superconductors separated by a thin insulator can be treated with the same theory [2, 43]. The quasiparticle current through S_1IS_2 junction, where S_1 and S_2 can be similar or dissimilar superconducting materials, is given by

$$I(V,T)=\frac{1}{eR_{\mathcal{T}}}\int_{-\infty}^{\infty}n_{S1}(E)n_{S2}(E+eV)[f_{S1}(E,T)-f_{S2}(E+eV,T)]\mathrm{d}E. \qquad (2.6)$$

where n_{S_1} and n_{S_2} are the densities of states of the two superconductors 1 and 2. The $I-V$ characteristics of a S_1IS_2 tunnel junction is shown in Fig. 2.4. Here superconductor S_1 possesses a different energy gap than superconductor S_2. Such S_1IS_2 tunnel junctions also fall into the family of Josephson junctions, and their $I-V$ characteristics cannot be fully described in the quasiparticle tunneling framework (2.6), as there is additional supercurrent (Cooper-pair tunneling) branch at $V=0$.

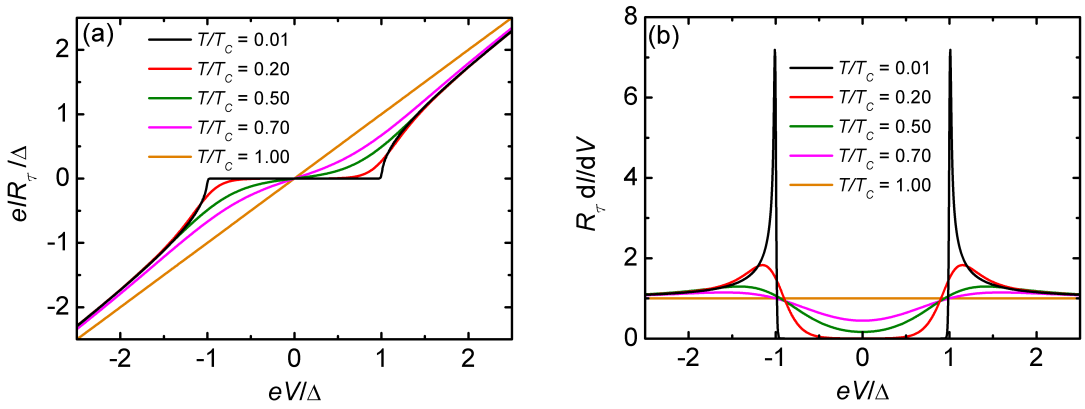

FIGURE 2.3 Calculated (a) current-voltage ($I-V$) and (b) differential conductance-voltage ($\mathrm{d}I/\mathrm{d}V-I$) characteristics of a NIS tunnel junction at different temperatures. The Dynes parameter was assumed to be $\Gamma' = 1\times10^{-4}$.

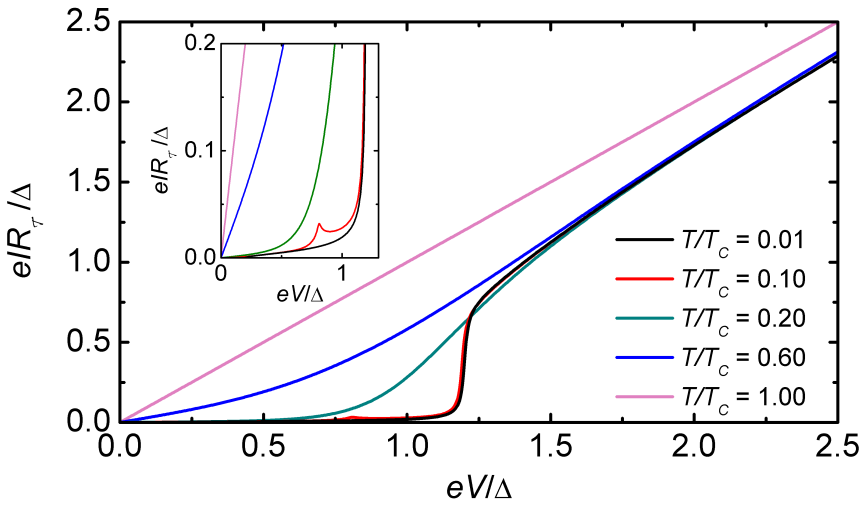

FIGURE 2.4 Calculated current-voltage characteristics of a S_1IS_2 tunnel junction at different temperatures. At low temperatures, the current exhibits strong features at voltages $(\Delta_1+\Delta_2)/e$ and $(\Delta_1-\Delta_2)/e$. The inset shows a small peak at $(|\Delta_1-\Delta_2|)/e$. Simulation was done assuming $\Gamma'_1 = 1\times10^{-2}$ and $\Gamma'_2 = 1\times10^{-4}$.

2.3 Josephson junctions

Originally, a Josephson junction [45] consisted of two superconducting electrodes separated by a thin insulating layer, but generally the term and theory of Josephson junctions are valid for other weakly coupled superconducting structures as well. Usually the term weak link describes certain types of junctions, which exhibit non-tunneling conductivity (by proximity effect) to distinguish them from the ordinary tunneling barrier junctions. A weak link between two superconducting electrodes can be normal metal, constriction, or a semiconductor interlayer so thin that wave-functions of superconducting electrodes overlap across the junction. [2, 29, 46].

The Josephson effect is a general feature of weakly linked superconductors and can be described in terms of the overlap of two quantum mechanical Ginzburg-Landau wavefunctions between these linked superconductors [2, 29, 46]. At zero voltages the manifestation of the effect is the Josephson supercurrent

$$I = I_C \ \sin\delta \tag{2.7}$$

where δ is the phase difference between two superconducting electrodes and I_C is the critical current, i.e. the maximum supercurrent, which reflects the strength of the coupling between the electrodes [2, 29, 46]. The critical current I_C of a Josephson junction is both dependent on temperature and the superconducting energy gap. The magnitude of I_C in the case of a SIS junction with symmetric gaps is given by the Ambegaokar-Baratoff relation [2, 32, 47]

$$I_C = \frac{\pi}{2} \ \frac{\Delta(T)}{eR_{\mathrm{N}}} \ \tanh\Big(\frac{\Delta(T)}{2k_BT}\Big) \tag{2.8}$$

where R_{N} is the normal state resistance of the junction at zero applied bias. Experiments have shown that materials with a low critical temperature follow equation (2.8) well [48]. Zero voltage DC properties of SIS Josephson junctions can be adequately described by equations (2.7) and (2.8) above.

The phase difference δ can evolve in time and is related to applied voltage difference V across the electrodes by [46]

$$\frac{\mathrm{d}\delta}{\mathrm{d}t} = \frac{2e}{\hbar}V. \tag{2.9}$$

Equation (2.9) describes the ac Josephson effect which gives oscillations to Josephson supercurrent with the angular Josephson frequency [32, 49]

$$\omega_J = \frac{2e}{\hbar}V, \tag{2.10}$$

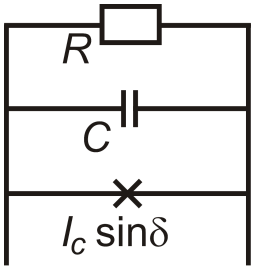

FIGURE 2.5 A circuit diagram equivalent to Josephson junction, where R is resistance and C capacitance.

while the current varies between values $-I_C$ and I_C. Equation (2.9) leads to

$$\delta(t) = \delta_0 + \frac{2e}{\hbar}\int V(t)\mathrm{d}t \tag{2.11}$$

where δ_0 is a constant representing the value of δ at time $t = 0$. For a constant applied voltage V, inserting the equation (2.11) into (2.7) leads to an oscillating (ac) current [32] of the form

$$I = I_C \sin(\delta_0 + \omega_J t) \tag{2.12}$$

with angular frequency $\omega_J = 2eV/\hbar$. With nonzero applied voltages, a DC quasiparticle current, described by the equation (2.6), also flows across the junction.

2.3.1 Josephson junctions with RCSJ model

For the finite voltage ac Josephson effect, a resistively and capacitively shunted (RCSJ) junction model gives a good phenomenological description for different kinds of Josephson junctions [2, 29, 32]. The circuit is illustrated in Fig. 2.5 where R is a shunt resistor, causing dissipation, and at finite voltage C is the geometry dependent shunting capacitance between the superconducting electrodes.

In the RCSJ model, current flows in three parallel channels, and the total current through the junction is given by [32]

$$I = I_C \sin\delta + \frac{V}{R} + C\frac{\mathrm{d}V}{\mathrm{d}t} \tag{2.13}$$

Eliminating V from equation (2.13) and using Eq. (2.9) we get

$$I = I_C \sin\delta + \frac{\hbar}{2eR}\frac{\mathrm{d}\delta}{\mathrm{d}t} + \frac{\hbar C}{2e}\frac{\mathrm{d}^2\delta}{\mathrm{d}t^2} \tag{2.14}$$

Defining a new scaled time parameter

$$\tau = \frac{2e}{\hbar} I_C R t \tag{2.15}$$

and dividing equation (2.14) by I_C leads to

$$\frac{I}{I_C} = \sin\delta + \frac{d\delta}{d\tau} + \beta_C \frac{d^2\delta}{d^2\tau} \tag{2.16}$$

where β_C is the so-called McCumber-Stewart damping parameter [50, 51]

$$\beta_C = \frac{2e}{\hbar} I_C C R^2. \tag{2.17}$$

A Josephson junction is called overdamped when C is so small that $\beta_C < 1$, whereas underdamped junctions have $\beta_C > 1$ [2].

Negligible capacitance ($C = 0$) leads to $\beta_C = 0$ and DC $I - V$ characteristics showing a parabolic dependence when $V \neq 0$ [32], as illustrated in Fig. 2.6. The situation $\beta_C \to \infty$ represents ohmic behavior with resistance R. From Fig. 2.6 it is clearly seen that for each value of current, a value of voltage is uniquely defined.

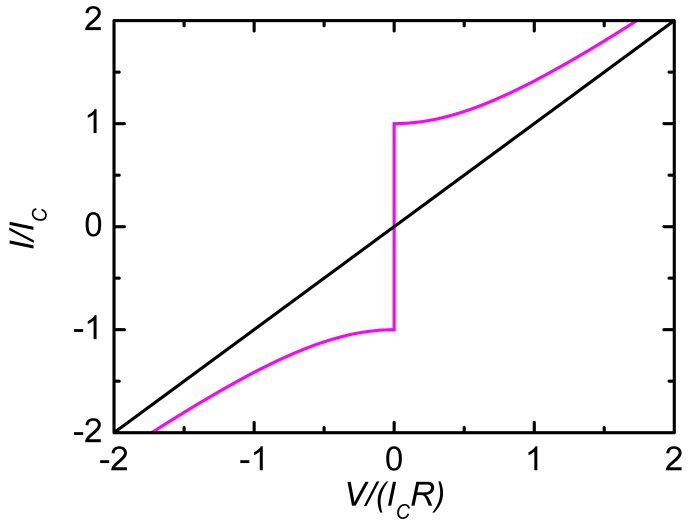

FIGURE 2.6 $I - V$ characteristic of a resistively shunted Josephson junction. The purple curve $\beta_C = 0$ (negligible small capacitance), while the black curve represent $\beta_C = \infty$ (capacitance domination).

$I - V$ characteristics of a Josephson junction with $\beta_C \neq 0$ become more complex, and underdamped junctions ($\beta_C > 1$) actually exhibit hysteretic behavior [2, 32], a situation illustrated in Fig. 2.7. At the certain current ranges there are two

values of voltage for each current value, and the value of voltage in those ranges depends on history.

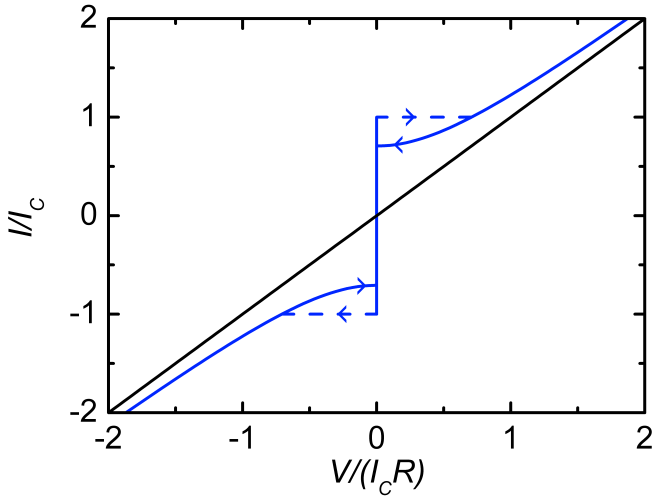

FIGURE 2.7 $I-V$ characteristic of a Josephson junctions exibiting hysteretic behaviour with $\beta > 1$ (blue curve) compared to $\beta_C = \infty$ (black curve). Arrows show direction of change of bias current, dashed lead is a jump.

2.3.2 Josephson junctions with RSJ model

Typically, tunnel junctions exhibit high values of capacitance, leading to $\beta_C \gg 1$. However, in contrast to SIS tunnel junctions, the majority of weak links exhibits $\beta_C \ll 1$, where R depends on the size of weak link. Weak links with $C \approx 0$ obey the RSJ model [2,29,32]

$$I = I_C \sin\delta + \frac{V}{R} \tag{2.18}$$

One class of weak links are superconductor/normal metal/superconductor (SNS) junctions. In these junctions, Josephson current is a result of coupled wavefunctions via the so-called proximity effect. The conventional proximity effect theory is based on BCS theory of superconductivity [2,32,48]. These SNS non-tunneling weak links exhibit naturally the non-hysteretic single valued current-voltage characteristics, required for rapid single flux quantum logic. Such characteristics are also possible for tunnel junctions with intrinsically high capacitance, but then an external shunt resistor is needed to damp the junctions.

2.3.3 The proximity effect and Andreev reflection

In a situation where electrical current passes or penetrates the interface from normal metal to the superconducting side, a certain fraction of electrons are transferred as supercurrent and rest end up as a nonequilibrium charges, which relax into supercurrent over a certain distance [2].

The behaviour of electrons incident on the superconductor from the normal metal side depends upon the features of interface between the two electrodes. The clean SNS junctions do not exhibit a barrier between the electrodes, so the current transfer process is described by the Andreev reflection theory [2, 52, 53]. At the interface an incident electron with energy $E \gg \Delta(T)$ enters the superconductor as nonequilibrium quasiparticle. An electron incident on a superconductor with energies $E < \Delta(T)$ cannot enter directly into the superconductor as a quasiparticles since in the ideal situation there are no available states inside energy gap. However, the electron can follow the Andreev reflection process, whereby the incident electron is reflected back to normal metal as a hole and a charge $2e$ is transferred into Cooper pair condensate. This event is illustrated in Fig. 2.8. The Cooper pairs can also leak to the normal metal via an opposite process, whereby a correlated quasielectron and a quasihole pair is created in the normal conductor. This process of superconducting properties leaking into a normal metal is called the proximity effect. In addition, the inverse proximity effect can also be applied to diminish the superconducting properties of a material [54].

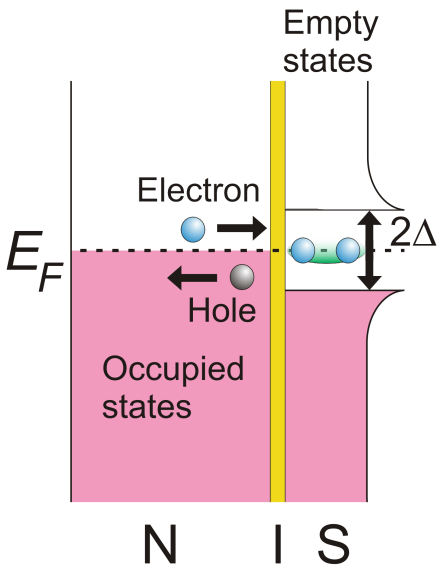

FIGURE 2.8 Andreev reflection of an electron-hole pair at the SN interface with an occupation diagram schematics. Figure adapted from Ref. [53].

2.3.4 Likharev's theory for critical current of SNS junctions

Ambegaokar-Baratoff equation (2.8) gives a general expression for temperature dependent critical current I_C for SIS Josephson junctions. In contrast, for SNS junctions the Cooper pairs leak from the superconductor into the normal electrode as discussed in subsection 2.3.3, and Eq. (2.8) is not valid.

In an SNS junction, the density of Cooper pairs in the normal metal decreases with distance from the superconducting interface [32]. This spatial decay of Cooper pairs is approximately exponential, and the distance where the density has decreased by a factor 1/e compared to density of Cooper pairs in superconductor is called as the coherence length of a normal conductor [32], which is expressed as

$$\xi_{\mathrm{N}} = \sqrt{\frac{\hbar D}{2\pi k_B T}} \tag{2.19}$$

where D is the diffusion constant given by

$$D = \frac{1}{e^2 N_{\mathrm{N}}(E_F)\rho} \tag{2.20}$$

and $N_{\mathrm{N}}(E_F)$ is the density of states at Fermi energy, and ρ is the resistivity of the normal conducting layer.

The proximity effect based theory for SNS junctions [29] was developed by Likharev for the temperature range $0.3 \times T_C < T < T_C$. Within that range and with the limiting condition [48] that the normal layer thickness $L > 2\xi_{\mathrm{N}}(T_C)$, Likharev's theory agrees fairly well with the earlier work of de Gennes [55] for SNS junctions. Likharev's theoretical expression for the critical current I_C of the SNS junction when $0.3 \times T_C < T < T_C$ is

$$I_C(T,\ L) = \frac{2}{\pi e R_{\mathrm{N}}} \frac{|\Delta|^2}{k_B T_C} \frac{L/\xi_{\mathrm{N}}}{\sinh(L/\xi_{\mathrm{N}})}, \tag{2.21}$$

where R_{N} is the resistance of the normal layer. This Eq. (2.21) can be further simplified for $L \gg \xi_{\mathrm{N}}$ as

$$I_C(T,\ L) \approx \frac{4}{\pi e R_{\mathrm{N}}} \frac{|\Delta|^2}{k_B T_C} \frac{L}{\xi_{\mathrm{N}}}\, \mathrm{e}^{-L/\xi_{\mathrm{N}}}. \tag{2.22}$$

2.3.5 Josephson junctions under the influence of magnetic field

If a Josephson junction device is placed in an applied magnetic field that is perpendicular to a current flow, the magnetic flux inside the junction, the current, and field

vary laterally over a certain distance called Josephson penetration depth [32,48]:

$$\lambda_J = \sqrt{\frac{\Phi_0}{2\pi\mu J_C(d+2\lambda_L)}} \tag{2.23}$$

where $\Phi_0 = h/(2e)$ is a magnetic flux quantum, μ represent permeability of the barrier layer (N or I), J_C is the critical current density, d is the thickness of the barrier layer, and λ_L is the London penetration depth of superconducting electrode, characteristic to each superconducting material.

It should be noted that if the width of the junction is greater than λ_J, then the screening effects of the Josephson current cannot be neglected, producing non-uniform current density. However, non-uniformities can be neglected if the width of junction smaller than λ_J. In that case, the critical current I_C of a rectangular Josephson junction has a certain response to the external magnetic flux (Φ), when the magnetic field penetrates the junction in direction perpendicular to the current flow [32,48]. The response known as the Fraunhofer pattern [32,48], and is given by

$$I_C(\Phi) = I_C(0)\left|\frac{\sin(\pi\Phi/\Phi_0)}{(\pi\Phi/\Phi_0)}\right| \tag{2.24}$$

and is illustarated in Fig. 2.9. The periodic structure of the critical current with increasing magnetic flux is clearly seen. The uniformity of tunneling current for rectangular junction can typically be tested [32,48] by measuring $I_C(\Phi)$ and comparing to the expected Fraunhofer pattern.

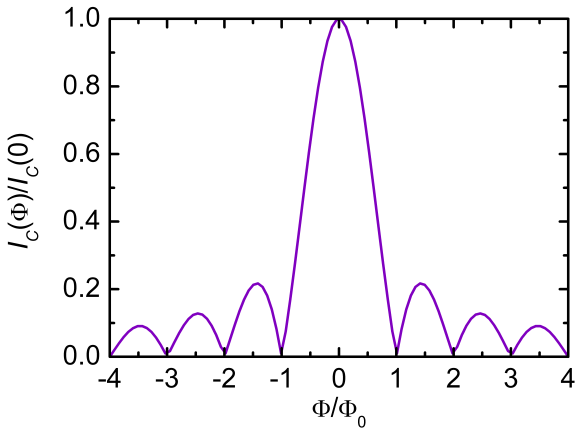

FIGURE 2.9 The Fraunhofer pattern describing the periodic shape of the critical current I_C with the increasing magnetic flux.

2.3.6 Rapid single flux quantum logic

Rapid single flux quantum (RSFQ) logic dates back to 1985 when Likharev et al. [56] suggested a new perspective to Josephson junction based computing. In contrast to semiconductor transistor and superconducting latching logic, where binary information is presented as DC voltages, in RSFQ logic information is presented by ∼picosecond (ps) long voltage pulses $V(t)$ of a quantized area [27]

$$\int V(t)dt = \int \frac{\hbar}{2e}\,\mathrm{d}\delta = \frac{h}{2e} = \Phi_0 \approx 2.07\,\mathrm{mV}\ \times \mathrm{ps}. \tag{2.25}$$

These single flux quantum pulses can be can be generated, numericized, amplified and reproduced in overdamped ($\beta_C \ll 1$) SNS junctions, which self-reset themselves back to the superconducting state after a current pulse.

RSFQ logic circuits consist mainly of three elements, which are inductors, current sources and Josephson junctions. Josephson junction circuits are biased in such a way that when a pulse propagates through the junction, the critical current of the Josephson junction I_C is exceeded, causing switching [27]. The maximum operating speed so far is up to 750-770 GHz [57, 58]. The operating speed is fixed by the time scale of the Josephson junction, and this time scale is determined by the $I_C R_\mathrm{N}$ product of the junction, since it is inversely proportional to SFQ pulse width [26, 59]. A full operation at 30-50 GHz frequency will need the $I_C R_\mathrm{N}$ product greater than ∼0.3 mV [26, 59].

The main advantages of superconducting electronics compared to traditional semiconductor based electronics are (i) significantly higher speed and (ii) lower operational power consumption. However, cooling the devices to the superconducting state and the vast financial investments needed for industrial scale productions are clear disadvantages and hindrances to RSFQ logic based devices.

2.4 Applications of the NIS junctions: thermometry and cooling

NIS based on-chip low temperature thermometry was carried out by Rowell and Tsui in 1976 for the first time [60]. Since then, NIS thermometers have been used in accurate low temperature thermometry in variety of applications to probe for example electron-phonon interaction, and electronic cooling, either with symmetric or asymmetric tunnel junctions [4, 5, 31, 41, 61–63].

2.4.1 NIS junctions as thermometers

The NIS tunnel junction current-voltage characteristic has strong temperature dependence especially for temperatures $T \lesssim 0.4 \times T_C$ [5]. The $I-V$ characteristics of a NIS junction are insensitive to temperature of superconducting electrode. However, the $I-V$ of NIS junction is very sensitive to the temperature of the electrons in the N electrode ($T_{\mathrm{N},e}$). This can be seen by using the mathematical expressions $f_i(-E) = 1 - f_i(E)$ and $n_{\mathrm{i}}(E) = n_{\mathrm{i}}(-E)$ [43], so that Eq. (2.5) can be expressed in a form:

$$I(V, T_{\mathrm{N},e}) = \frac{1}{2eR_T} \int_{-\infty}^{\infty} n_{\mathrm{S}}(E)[f_{\mathrm{N}}(E - eV, T_{\mathrm{N},e}) - f_{\mathrm{N}}(E + eV, T_{\mathrm{N},e})]\mathrm{d}E. \tag{2.26}$$

When a NIS junction is constant current biased, the voltage across the junction will change when the temperature $T_{\mathrm{N},e}$ changes. The principle of the NIS thermometry is illustrated in figures 2.10(a) and (b).

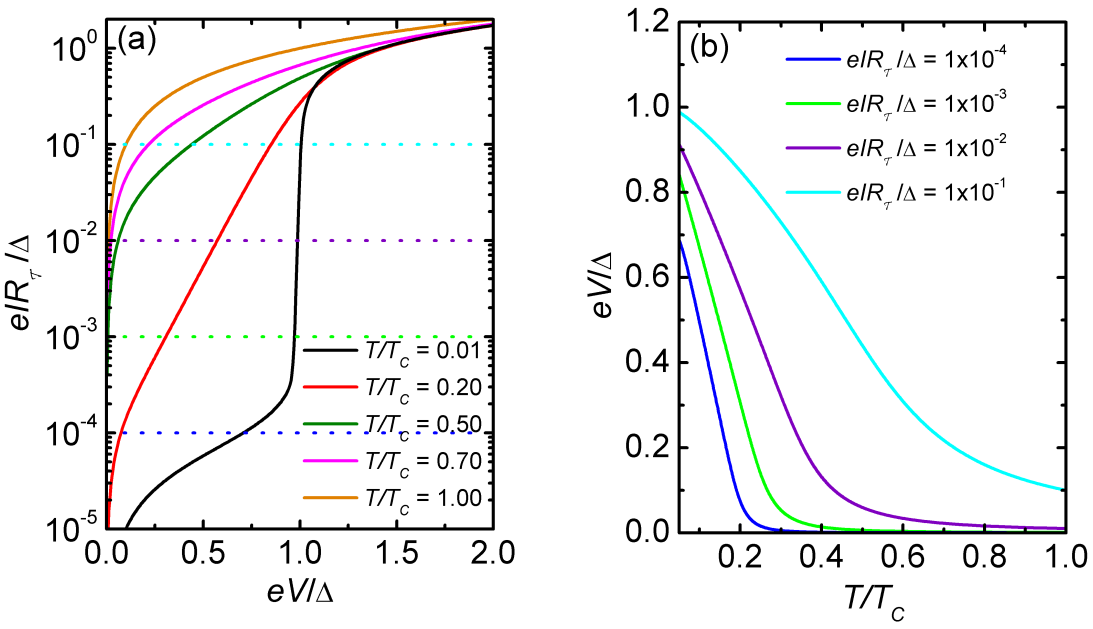

FIGURE 2.10 The principles of NIS tunnel junction thermometry. (a) Theoretical current-voltage characteristics of a NIS junction at several temperatures. When NIS junction is biased with a constant current $eIR_T/\Delta = 1 \times 10^{-4}$, 1×10^{-3}, 1×10^{-2} or 1×10^{-1} represented by horizontal dashed lines in (a), the corresponding voltage across the junction as a function of temperature has the form shown in (b). Thermometer sensitivity depends on biasing current.

The $I-V$ characteristics can be approximated at low voltages $0 \ll V \leq \Delta/e$ and at low temperature range $k_B T \ll \Delta$ as [39,64,65]

$$I(V,T) \approx I_0 \mathrm{e}^{\frac{eV-\Delta}{k_B T}} \tag{2.27}$$

where $I_0 = \sqrt{2\pi\Delta k_B T}/(2eR_{\mathcal{T}})$ and, thus the thermometer responsivity is

$$\frac{dV}{dT} \approx -\frac{k_B}{e}\ln\Big(\frac{I_0}{I}\Big). \tag{2.28}$$

By measuring the voltage V of a current biased thermometer, a direct information of $f_{\mathrm{N}}(E)$ is obtained. In principle $T_{\mathrm{N},e}$ can be obtained without any fitting parameters, by measuring the superconducting energy gap and tunneling resistance $R_{\mathcal{T}}$ beforehand. In practice, NIS temperature sensors are not practical primary thermometers, since each sample is unique with different characteristics and defects. It should be noted that $T_{\mathrm{N},e}$ may differ from the lattice phonon temperature in the N electrode due to a weak electron-phonon coupling at low temperatures [5, 41]. The NIS thermometers are also unsuited to thermometry in the presence of a strong magnetic field, which causes deviations to the behaviour of the superconductor and eventually quenches superconductivity [5].

2.4.2 NIS junctions as coolers

The fundamental property of cooling with an NIS junction is based on the existence of the superconducting energy gap, like in NIS thermometry [5,64]. Electronic cooling of the Cu normal metal electrode with Cu/AlO_x/Al NIS junction was first demonstrated by Nahum and co-workers in 1994 [65]. Two years later, Leivo et al. [63] noticed that by arranging two similar NIS junction in series, thereby forming a symmetric SINIS junction, cooling effect was enhanced. In addition to normal metal cooling, also dielectric membranes [66] and phonon systems [6,67] have been cooled with NIS junctions. Recent research shows that two asymmetric NIS junctions in series can lead to improved cooling characteristics [31]. So far, aluminium based large area junctions in the sub 300 mK range have successfully achieved cooling powers of ~ 50 pW [68].

At finite temperatures and under the application of an appropriate voltage, it is possible to selectively remove "hot" electrons from the normal metal into the superconductor through one junction. Via the other junction, quasiholes from the superconductor enter into normal metal below the Fermi level [5]. Both these tunneling processes generate cooling by reducing the average energy of the normal metal. The tunneling events and operation of a SINIS cooler are illustrated in Fig.

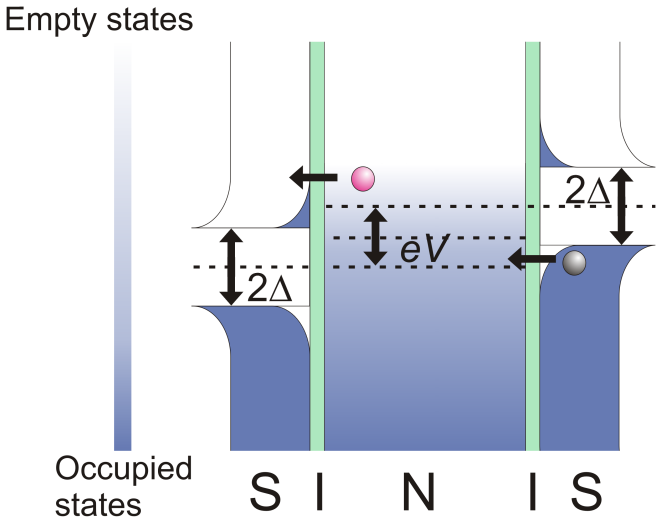

FIGURE 2.11 In the SINIS cooler the average energy of the normal metal electrons is reduced when "hot" electrons tunnel out of the normal metal and "cold" quasiholes tunnel into the normal metal. Figure adapted from Ref. [39].

2.11. The quasielectrons extracted from the normal metal carry out energy and relax near the junction [39]. These electrons can also to tunnel back to the normal metal so that some way of trapping the quasiparticles is beneficial. For example a large normal metal in contact with the junction area works well as a quasiparticle trap [69].

The cooling power of an ideal NIS junction is given by [31,63]

$$\dot{Q}_{\mathrm{NIS}}(V,T_{\mathrm{S},e},T_{\mathrm{N},e}) = \frac{1}{e^2R_{\mathcal{T}}}\int_{-\infty}^{\infty}(E+eV)n_{\mathrm{S}}(E)[f_{\mathrm{S}}(E,T_{\mathrm{S},e})-f_{\mathrm{N}}(E+eV,T_{\mathrm{N},e})]\mathrm{d}E \quad (2.29)$$

which depends both on the temperature of the superconductor and the normal metal. The cooling power is maximum when $T \approx 0.4 \times T_C$ and the applied bias $V \lesssim \Delta/e$ [19,39,63,66], in which case

$$\dot{Q}_{\mathrm{max}} \approx 0.6 \times \frac{\Delta^2}{e^2R_{\mathcal{T}}}\left(\frac{k_BT_{\mathrm{N},e}}{\Delta}\right)^{3/2}. \quad (2.30)$$

From equation (2.30) it is clear that maximum cooling power can be enhanced by increasing the energy gap Δ value and/or decreasing the tunneling resistance of a device. This makes Nb one of the desired materials for cooler applications. The tunneling resistance is usually decreased by increasing the size of cooler junctions [A.IV], [41,69], but barrier material manipulation towards increasing transparency is also possible.

For more accurate characterisation of a NIS cooler, self cooling and heating effects should be included. Thus in dynamic equilibrium, the cooling should balance

heating, which leads to the equation [31,70]

$$\dot{Q}_{\mathrm{NIS}} = A(T_{Bath}^{n} - T_{\mathrm{N}}^{n}) + \mathcal{B}\left[\dot{Q}_{\mathrm{NIS}} + IV\right]. \tag{2.31}$$

The coupling strength constant A is given by $A = \Sigma\Omega$, where Σ is the electron-phonon coupling constant and Ω is the normal metal electron gas volume. The exponent n = 5 for good metals with thickness > 30 nm. The latter term $\dot{Q}_{\mathrm{NIS}}+IV$ in equation (2.31) describes power dissipation in the superconducting electrode. The term $\mathcal{B}(\dot{Q}_{\mathrm{NIS}} + IV)$ with $0 \leq \mathcal{B} \leq 1$ then corresponds to that fraction of the total heat, which is taken back by normal metal via backflow. Heat flows back from the superconductor into normal metal for example due to tunneling of quasiparticles, or when normal the metal absorbs phonons released by quasiparticle recombination. Joule heating in the cooling and heating balance formula (2.31) is very small and can be neglected if copper is used as a normal metal [31].

The intrinsic broadening of the density of the states of the superconductor, characterized by the Dynes parameter, also has an impact on the cooling power. The theoretical variation of the cooling power of a NIS device for different Dynes values, as a function of applied voltage bias, is shown in Fig. 2.12.

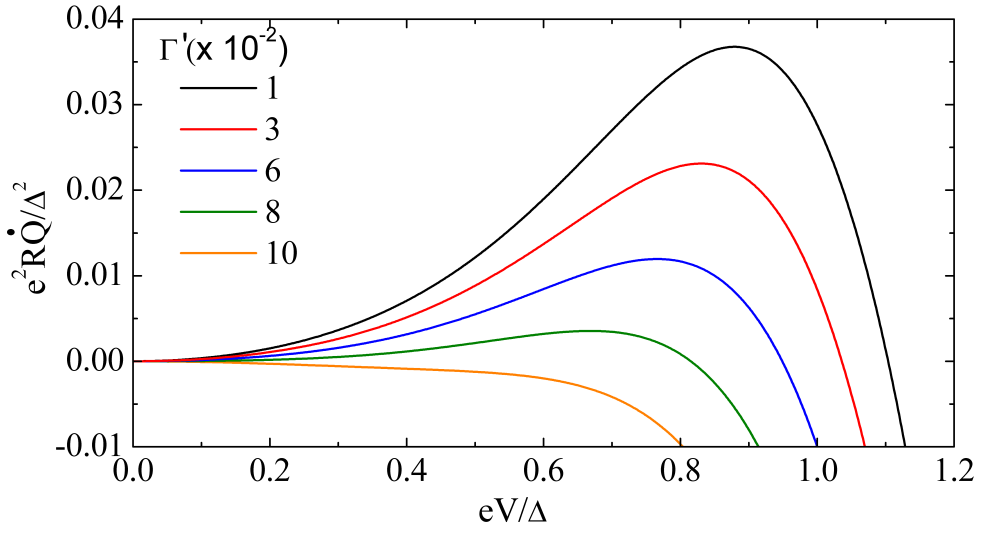

FIGURE 2.12 Variation of the cooling power of a NIS junction with voltage for various values of Dynes parameter $\Gamma' = \Gamma/\Delta$. The results were calculated theoretically assuming temperature of $0.3 \times T_C$. Figure adapted from Ref. [A.III].

Chapter 3

Experimental techniques and theory of thin film growth

In this chapter, the experimental techniques used to fabricate and study the NIS and SNS junctions are briefly discussed. A short introduction to pulsed laser deposition, thin film growth, electron-beam lithography and other methods used in the sample fabrication and measurements are briefly mentioned.

3.1 Pulsed laser deposition

In the last 20-25 years pulsed laser deposition (PLD) has emerged as a promising and intrinsically simple technique for thin film deposition of various materials [71–73]. The technique has received broad experimental development after the discovery of successfull deposition of high-T_C films, but in principle pulsed laser deposition can be applied to any material available in solid form [71,74,75].

The main advantages of this cost-effective, relative fast and conceptually simple process are (i) the possibility of successful deposition of chemically complex materials for example oxides [76] and high T_C thin films [74,75], (ii) reactive growth of multicomponent films, and (iii) efficient stoichiometry transfer from a substrate to an ablated film [A.II], [71]. Especially (i) and (iii) are advantages of PLD over sputter deposition. Another process used to thin film deposition is a molecular beam epitaxy (MBE), but it is slow and expensive [72].

In spite of the conceptual and experimental simplicity of PLD, the ablation process itself is complex, and a successful deposition of a film needs precise tuning of the deposition parameters. In an ablation process, shown in Fig. 3.1, laser pulses are focused through a glass window to a rotating and usually solid target (for example niobium metal) in an ultra-high vacuum or ambient high-purity gas environment.

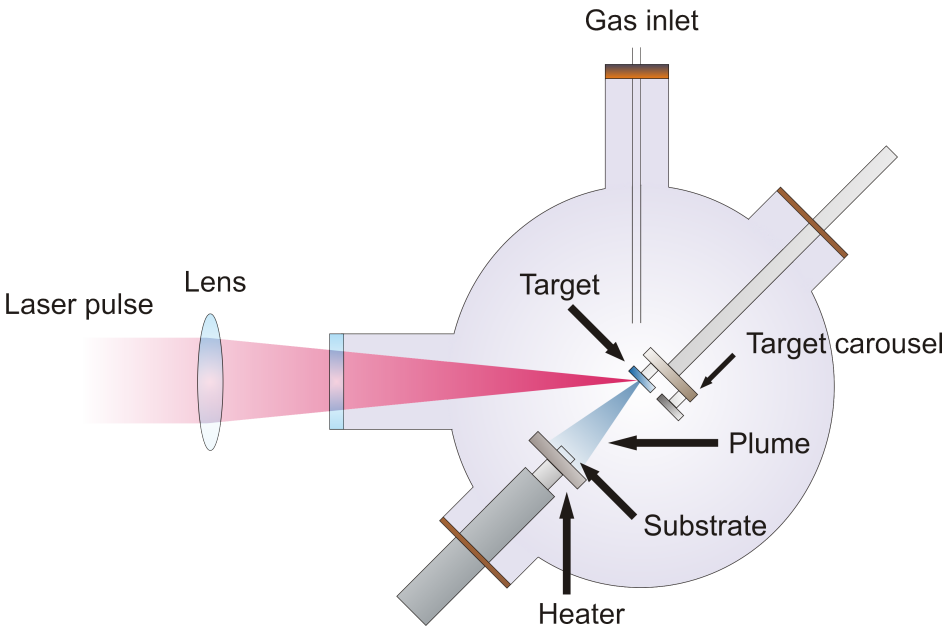

FIGURE 3.1 A shematics of a pulsed laser deposition system.

In general, the ablated material is deposited onto a heated substrate [71–73]. Using a multi-target carousel, multi layered films can be deposited *in situ*.

3.1.1 Thermal cycle

When a short nanosecond laser pulse interacts with the surface of a target, the result is the absorption of the radiation, up to a certain depth depending on the material [71–73,77]. If the binding energy of an atom on the target surface is exceeded by the delivered energy, an ablation of the atom occurs. The laser pulse interaction with the target surface can be divided to different categories defined by the laser pulse width.

When a nanosecond laser pulse is incident on a target, free electron excitations are created via the absorption of radiation and collisions. A part of the incident energy is transferred to the crystal lattice via electron-phonon coupling [71–73, 77]. This energy transfer into metal can be more closely described by a heat diffusion model [71,77–79].

In the vicinity of the target surface, neutral atoms, molecules, energetic electrons and other particles collide with each other to form a dense high pressure plasma (plume), which starts expanding rapidly. In vacuum, this plume expands adiabatically, but in an ambient gas environment (e.g. N_2), particles of plume scatter and form compounds and molecules by a thermalization process [71–73,80,81]. With different background pressures, diverse compounds with characteristic properties

can be deposited. The resulting thin films can have various crystalline qualities, for example epitaxial, single-crystal, polycrystalline or amorphous. Figure 3.2 shows a simplified thermal cycle.

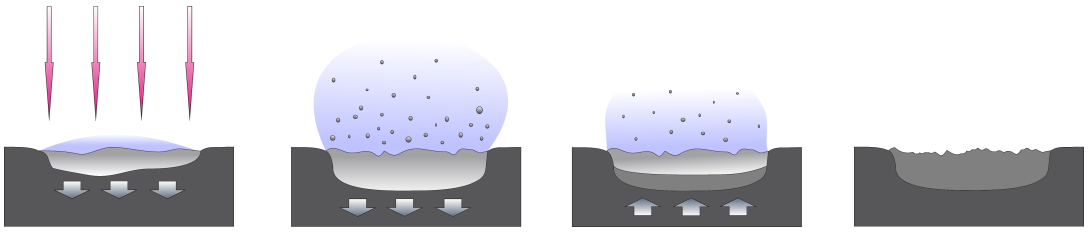

FIGURE 3.2 An illustration of a basic thermal cycle induced by short laser pulses. Starting from left, the laser pulse hits and is absorbed by the material, resulting in melting of the target surface followed by vaporisation. Next, the melting propagates deeper and vaporization continues. Then the melt front stars to recede and finally the surface of the target is resolidified. Subsequent incident laser pulses will interact with the resolidified surface material, where altered topography may effect the plume behaviour. Figure adapted from Ref. [71].

3.1.2 Nd:YAG and excimer lasers

One of the main advantages of PLD is that the lasers are independent of the overall deposition system. Inside the deposition chamber, targets and different background gases can be changed *in situ*. Although excimer lasers are the dominant choice for PLD, solid state lasers can also be employed. Compared to an excimer laser the main advantages of a solid state laser are the lower operating costs and the lack of toxic gas hazards. However, excimer lasers surpass the output powers of solid state lasers in the ultraviolet regime, but solid state lasers can be used for ablation in the infrared region [A.II].

In Nd:YAG lasers, Yttrium Aluminium Garnet (YAG) serves as a host for neodynium (Nd) impurity ions [71]. Electrons in the doped impurity Nd ions are exited optically to higher energy states via an external source. The lasing is generated when exited states relax to ground state. The Nd:YAG lasers have excellent long term stability and they are ideal lasers for thick film deposition [71].

For solid state Nd:YAG lasers, the fundamental wavelength is 1064 nm and film deposition using such radiation is possible [A.II]. Usually frequency doublers and other optics are employed to generate and separate out a 532 nm pulse from the primary pulse, but this results in significant loss in the output pulse energy of the 532 nm radiation. Additional frequency multipliers and optics can be used, since

most of the target materials exhibit strongest absorption spectral region between 200-400 nm [71].

Excimer (excited dimer) lasers operate in the ultraviolet region, for example the KrF laser at 248 nm [A.I]. The excimer molecules consist of gaseous mixture of three components: rare gas (Xe, Kr, Ar), halogen (Cl_2 or F_2) and Ne or He as a buffer gas (represented with letter B in the following). The halogen gas molecule combines with the noble gas atom, forming for example KrF, ArF, XeF and XeCl [71]. When energy is pumped into the gas mixture, a sequence of ionic and electronically exited states leads to the formation of excimer molecules, usually dimers. Lasing in these gas laser systems is based on the photon excitation from the of rapidly dissociative, repulsive ground state to the bound upper electronic state of the excimer molecule [71]. Excited molecules emit photons while relaxing to the repulsive ground state, and the dimer molecules dissociate rapidly to unbound atoms, thereby being available for the next lasing cycle.

For KrF lasing cycle, the positive and metastable inert gas ions are created first, followed by the negative halogen ion production. Then KrF^* metastable ions are formed. Finally KrF^* dissociates to separate atoms and are ready for a new cycle [82, 83]:

$$\begin{aligned} \mathrm{Kr} + e^- &\rightarrow \mathrm{Kr}^+ + 2e^- \\ \mathrm{Kr} + e^- &\rightarrow \mathrm{Kr}^* + e^- \\ \mathrm{F}_2 + e^- &\rightarrow \mathrm{F}^- + \mathrm{F} \\ \mathrm{Kr}^+ + \mathrm{F}^- + \mathrm{B} &\rightarrow \mathrm{KrF}^* + \mathrm{B} \\ \mathrm{Kr}^* + \mathrm{F}_2 &\rightarrow \mathrm{KrF}^* + \mathrm{F} \end{aligned}$$

Lasing : KrF^* + $h\nu'$ (stimulated emission)$\rightarrow$ Kr + F + $2h\nu$ (λ= 248 nm).

3.1.3 Drawbacks of PLD

In the simplest case, the PLD process can be described with a cyclic process consisting of four repetitive steps starting with vaporization of the target material, formation and propagation of the plume and the film growth [71, 73]. The basic thermal cycle of surface modification consist of four steps presented in Fig. 3.2. Pulsed photon bombardment of the target eventually causes particle ablation or desorption of the target surface, thus the energy of the laser pulse is transferred to kinetic energy of emitted particles [71, 73]. Laser-irradiated surfaces undergo physical and chemical changes resulting in ridges, ripples and cone formations [71, 73].

The two main characteristics which have limited the use of PLD are splashing

of particulates and the difficulty of obtaining uniform film thickness over a large area. These two drawbacks are challenges of PLD compared to sputter deposition and MBE. During the PLD process, particulates with diameters ranging from $\sim$0.1-10 μm can emerge from the solid, liquid or vapor state. Most particulates are approximately smaller than 1 μm, the smallest being formed in the vapor state [71,73]. Particulates ejected from the vapor or liquid state are usually spherical, and the particulates ejected from solid are of irregular shape. In metal targets the particulates, usually called droplets, result from subsurface boiling, recoil ejection and exfoliation [71].

Particulates give extra concern during thin film growth, if the deposited film is to be processed later on micrometer or even smaller scale. The size of the particulates depends, for example, on the material and smoothness of the target surface, the laser wavelength, the energy density and the ambient gas pressure [71,73]. Several simple experimental techniques can be applied to reduce the number and size of particulates. The easiest methods employed are (i) usage of short wavelenght lasers, (ii) suitable geometrical orientation between the target and a substrate, (iii) rotating target, and, (iv) maintaining a smooth target surface [71–73].

Strong forward peaking out of the target surface, and a narrow angular range are typical characteristics of the plume distribution [71,73]. Consequently, films with uniform thickness can be deposited only into a narrow angular range. Experimental solutions for this problem are laser beam rastering and a careful adjustment of the substrate relative to the target and the beam. In this way, uniform films of moderate dimensions can be deposited. An ambient background gas broadens the angular distribution, as does higher incident energy density and smoothness of the target surface [71–73].

3.2 Thin film growth

In this section, physical ideas of thin film growth are described in a qualitative way rather than using a complete quantitative mathematical formulation.

The process of thin film growth on a substrate from atoms deposited from gas phase is dominated by the competition between kinetic and thermodynamic processes. The simplest description of this non-equilibrium phenomenon on an atomistic level is the terrace-step-kink (TSK) model [84]. The fundamental elements of this model of film formation are described in Fig. 3.3. In thin film growth, the most important kinetic process is the diffusion of an adatom on a flat substrate surface, or the diffusion onto a terrace of ordered atoms [71, 84]. Sufficient surface mobility is needed to form smooth and uniform films. At a fixed deposition rate, the surface dif-

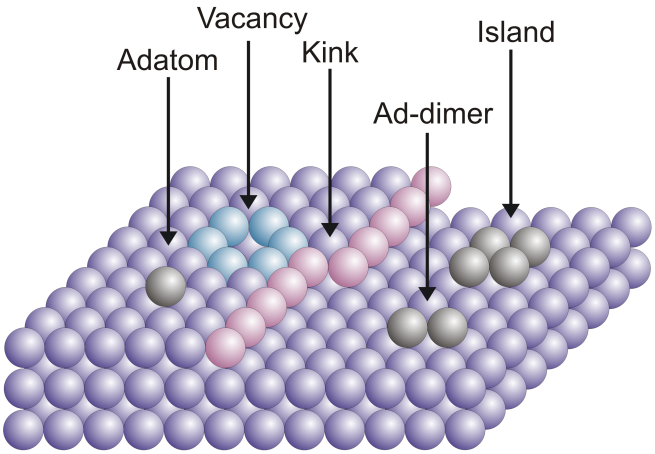

FIGURE 3.3 The basic entities of the terrace-step-kink (TSK) model on the surface of a simple cubic crystal. Figure adapted from Ref. [84].

fusion constant determines the average distance which an adatom will have to travel on the surface before joining with another adatom (forming ad-dimer), and possibly initiating an island nucleation, or uniting with an already existing island [84].

When more and more atoms join an island, the cohesive energy between atoms prevents the island from dissociating. On the surface islands develop specific morphologies and shapes (squares, triangles, hexagons, fractal-like or highly anisotropic), depending on atomic diffusion along island edges, bonding geometry and substrate crystal orientation [84].

By increasing the substrate temperature, atoms can be evaporated from a step onto a terrace, and atoms can also be ejected from a kink site. Moreover, corner atoms of an island may be removed and vacancies form, eventually leading towards a diffusion of the whole island [84].

Hence, the uniformity of an island of atoms in the horizontal direction is controlled by surface diffusion. The other important process in thin film growth is the interlayer mass transport, which controls the uniformity of three dimensional islands or layer of atoms in the vertical direction [84].

Surface processes such as diffusion, adsorption, re-evaporation and condensation of individual atoms determine the initial steps of film growth of ablated atoms [71, 72, 84]. These surface processes, which lead to the formation of a cluster and a film in the final macroscopic state, depend for example on chemical bonding, surface roughness and other processes, as illustrated in Fig 3.4.

A general theory of the film growth requires detailed rate equation for each process depicted in Fig. 3.4, although film growth processes can be described very well phenomenologically [53, 71]. Individual atoms in an assembly determine the

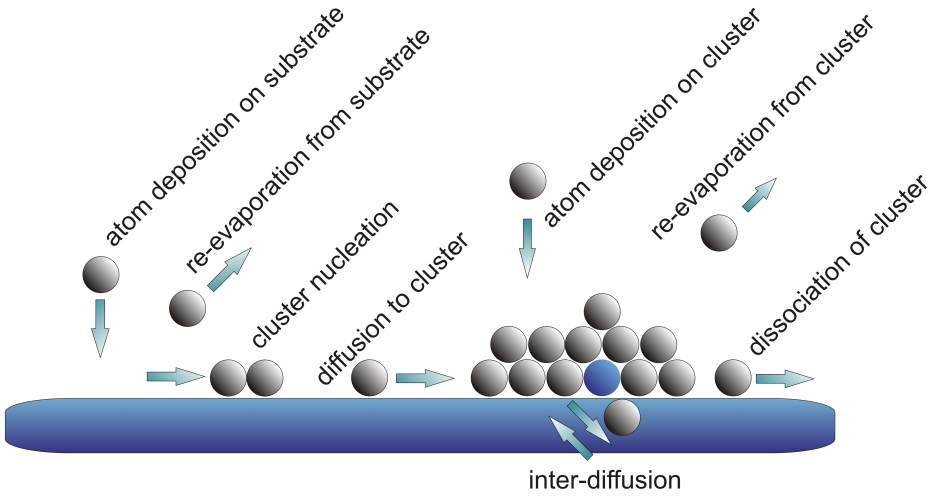

FIGURE 3.4 The atomic processes during nucleation of a three-dimensional atomic islands. Figure adapted from Ref. [71].

total free energy of the cluster, which further determines whether the cluster will undergo growth or dissolution. Three conventional, and markedly different modes of film nucleation and growth on clean plane surface exists. They are: the island growth (Vollmer-Weber) mode, the layer-by-layer growth (Frank-van de Merve) mode and the layer-plus-island growth (Stransky-Krastanov) mode [53,71,72,84–86]. Thin film growth modes are depicted in Fig. 3.5.

In the island growth mode, separate three dimensional islands of atoms are formed on the substrate surface, when interaction between the neighbouring atoms is stronger than the film-substrate interaction. From the experimental point of view, the island growth can be enhanced by decreasing the substrate temperature and by increasing the deposition rate [71,77]. The island growth mode is typical for metals deposited on insulators [53]. Despite the formation of separate islands during the initial steps of film growth, a continuous film appears at the end beyond a certain thickness [83]. For the island growth mode, the sum of the surface free energy of the film (σ_f) and the free energy of the interface (σ_i) is larger than the free energy of the substrate (σ_s) [53,86]

$$\Delta\sigma = \sigma_f + \sigma_i - \sigma_s > 0. \tag{3.1}$$

In the layer-by-layer growth mode, the strength of the interaction between the substrate and an atom layer exceeds the interaction between neighbouring atoms ($\Delta\sigma \leq 0$), and the strong film-substrate bonding promotes full-monolayer nucleation [71]. During the layer-by-layer growth, the $(n+1)$th layer starts to grow after the nth full monolayer has been completed. This growth mode is observed dur-

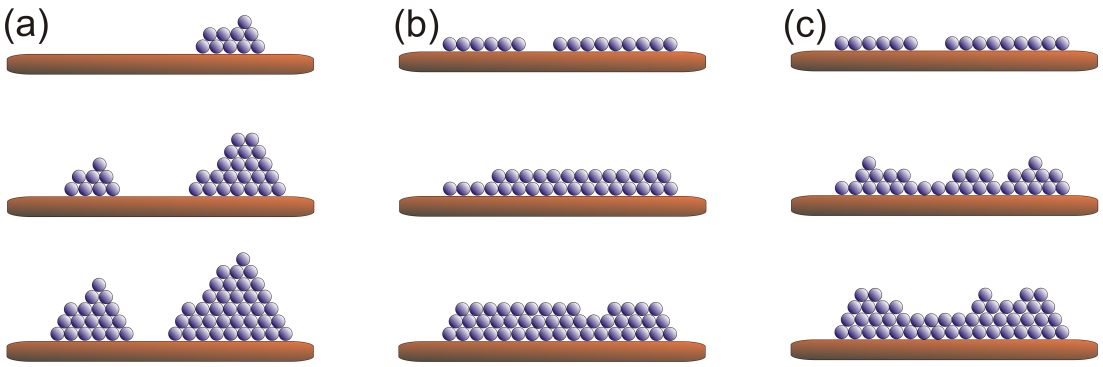

FIGURE 3.5 Three conventional growth modes of thin films on a plane surface (a) the island growth (Vollmer-Weber) mode, (b) the layer-by-layer growth (Frank-van de Merve) mode (c) the layer-plus-island growth (Stransky-Krastanov) mode. Figure adapted from Ref. [53].

ing epitaxial metal film growth [53, 86]. The layer-by-layer growth mode can be enhanced by increasing the temperature of the substrate and by keeping a moderate deposition rate [53, 77].

The layer-plus-island growth mode occurs when atomic clusters grow as three dimensional islands on top of monolayers. The sum of the free energies $\Delta\sigma$ can be smaller than zero below certain critical thickness, but larger than zero above, causing island growth [86]. This growth mode is observed when metals are deposited on semiconductors and is typical in a situation for large lattice mismatch between the deposited film and the substrate [53, 71].

3.3 Thin film deposition with UHV and PECVD systems

The thermal evaporation of metals by resistive or in electron-beam assisted heating are two of the most common ways to deposit a thin metal film in (ultra) high vacuum ($\sim 10^{-9}$ mbar) environment [5, 87]. In this thesis, metallization of aluminium (Al), copper (Cu) and niobium (Nb) were carried out in an ultra high (UHV) system, where the vacuum was achieved by an efficient cryopump. The crucible containing the metal in the UHV system was heated by a high-energy e-beam, which was guided by strong magnetic fields and focused onto a small region of the target metal. The thickness of the film was monitored with a quartz crystal-based high resolution thickness monitor.

In the plasma-enhanced chemical vapor deposition (PECVD), an rf discharge generates chemically reactive substances. This chemical vapor deposition process includes reactive gas flow in the vicinity of a heated substrate surface, where gases undergo thermally induced chemical reactions. Within this definition, the thermal oxidation of silicon in on oxygen environment is also one form of CVD [87].

In this thesis, the temperatures during SiO_2 and SiN deposition with the Oxford instruments PlasmaLab 80 plus PECVD system were 300°C, maximum [A.I]. SiO_2 and SiN are both excellent electrical insulators. In the growth process of SiO_2, highly poisonous silane SiH_4 in Ar (5 %) and nitrous oxide (N_2O) as an oxidizer were used as reactive gases. For silicon nitride growth process, SiH_4 in Ar (5 %) is used with ammonia (NH_3) and nitrogen N_2. In both deposition reactions, silane is used as the silicon source [87,88].

3.3.1 Electron beam lithography

The key elements of the electron beam lithography (EBL) process are the e-beam sensitive polymer based resists. These resists can be classified as negative or positive depending their response to the e-beam [87,89,90]. Conventionally, for a angle evaporation resists are used as double layers on the top of the substrate. The top resist layer is often polymethyl methacrylate (PMMA), and the bottom are polymethylmethacrylate methacrylic acid P(MMA-MAA) [89]. The bottom resist layer is much more sensitive to the e-beam, and hence backscattered electrons from the substrate will expose the underlying layer as well, forming an undercut. Sub $\sim$10 nm resolution is possible to achieve with e-beam lithography and PMMA [91]. Traditionally, the substrate is covered with the resist and spun to a desired thickness. After spinning, the substrate coated with the resists is baked on a hot plate at temperatures ≤ 170°C. The baking temperature should be based on the resist type and possible underlying metal layer on the substrate [92].

The e-beam lithography in this thesis was done with a scanning electron microscope LEO 1430, containing a lanthanum hexaboride filament as the thermal electron source and a motorized computer controlled stage. Under the e-beam exposure, scissions are formed in polymer chains of the positive resist, causing the exposed areas to dissolve in a developing solution [87,89,90,93]. For the the top layer, the developer consisted of a mixture of methyl isobutyl ketone (MIBK) and isopropyl alcohol (IPA) in a volume ratio of 1:2. The development time was $\sim$30-45 seconds. The developer for the bottom layer is a mixture of 2-methoxyethanol and methanol with a ratio 1:2 and the development time was $\sim$3-10 seconds. After each development, the substrate was rinsed with IPA and dried gently with helium or nitrogen.

The final metal structure was produced in lift-off with acetone, which dissolved the unexposed resist.

3.3.2 Plasma cleaning and reactive ion etching

Reactive ion etching (RIE) combines physical and chemical processes. The etching profile depends on the nature of the process and, the result can be either isotropic (usually chemical etching) or anisotropic (physical etching), but typically the etching process is a combination of both physical and chemical etching [87, 89, 90]. In a RIE system, dc or rf voltage is applied between two electrodes and, for a certain pressure and voltage, plasma is formed in gas environment between the electrodes. The etching rate depends on the specific parameters of each recipe (for example the nature of reactive gases, power, chamber pressure, geometry and etching time) and etched material [87]. Different materials have typically different etching rates, which allows selective etching of a material on the same substrate and the usage of masking layers. During the process of chemical etching, gases react with the substrate forming short lived and intermediate compounds. Pure physical etching is equivalent to sputtering by particle bombardment. The RIE system of Oxford Instruments Plasmalab 80 plus was used in this thesis.

3.3.3 Sputtering

Sputtering is the removal of atoms on the target surface via bombardment of incident energetic particles [94]. Physical sputtering is a practical tool for cleaning of surfaces [A.I], studying depth profiles by subsequent serial sectioning, and deposition thin films of different materials [B.II], [95].

3.3.4 Measurements at low temperatures

Measurements with SNS-junctions from 4.2 K to $\sim$16 K were performed with a dipstick type probe, which was precooled in liquid nitrogen before a slow immersion into a ^{4}He vapour or liquid. A ^{3}He$-^4$He dilution refrigerator was used to measure the SINIS based tunnel junction characteristics.

Operation of ^{3}He$-^4$He dilution refrigerators is based on the ^{3}He$-^4$He phase diagram [1]. Typically base temperatures of 40-80 mK is reached with the type of a refrigerator [96] used in this thesis. At low temperatures below 1 K, ^{3}He$-^4$He mixture may exist in three different states, fully normal fluid, fully superfluid or fluid with two separate phases on top of each other [1, 39, 96]. In the state with two phases, the top phase is a ^{3}He rich (concentrated) phase with a lower density, and the

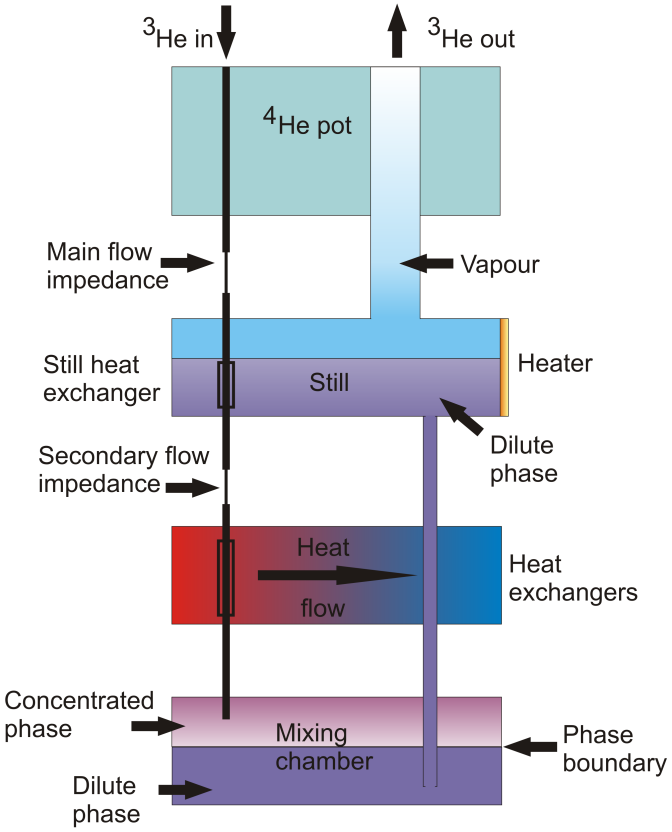

FIGURE 3.6 A schematic illustration of the ^{3}He$-^4$He dilution refrigerator, the main parts and operations are named. Figure adapted from Ref. [1].

bottom a ^{3}He poor (dilute), heavier phase. The separation of the ^{3}He$-^4$He mixture into two phases depends on the temperature and atomic concentration of ^{3}He. If the ^{3}He$-^4$He mixture is separated in two phases, then even at zero temperature ^{3}He poor phase contains $\sim$6.4 % of ^{3}He atoms [1,39].

The basic principles of dilution refrigerator operation is illustrated in Fig. 3.6. Flowing through the condenser and the main flow impedance, the incoming ^{3}He gas is liquefied and precooled to $\sim$1.2 K. Heat exchangers cool down ^{3}He further, and re-evaporation is prevented by a secondary flow impedance. Cooling occurs when ^{3}He atoms are transferred from the ^{3}He rich phase to the ^{3}He poor phase, where energy needed for the phase transition is taken from surrounding environment [1, 39]. Due to external pumping of ^{3}He atoms at the still chamber, and the temperature difference between the mixing and the still chamber, an osmotic pressure gradient drives liquid from ^{3}He poor phase through the heat exchanger to the still chamber, where ^{3}He atoms are pumped out, and the chamber is kept heated to maintain the requisite circulation rate [1,39,96].

The measurement lines of the dilution refrigerator had two RC filters, one at 4 K and the other at 60 mK. Microwave filtering between the resistor-capacitor (RC) filters was achieved with the help of Thermocoax cables [97]. Inside the refrigerator, the temperature of sample stage was monitored with Ruthenium oxide (RuO) thermometer (Lake Shore Cryotronics). Preamplifiers Ithaco (1211/1201) Low Noise were used to amplify the current and voltage signals. Measured data was delivered out of shielded room by optical fibres and collected by a computer using a LabVIEW based program.

Chapter 4

Pulsed laser deposition of niobium nitride thin films and device fabrication

This chapter describes the PLD of NbN thin films. In addition, specific sample fabrication details of Nb based SINIS and NbN based SINIS and SNS devices are provided.

4.1 Nitrides of niobium and tantalum

As members of transition metal nitride family, nitrides of niobium and tantalum can feature excellent combination of properties such as high melting point, extraordinary hardness, first-rate thermal and electrical conductivities, outstanding mechanical and considerable chemical stability, except to hydrofluoric acid and oxidizing acids and agents [98].

4.1.1 Nitrides of niobium

A substantial amount of interest and attention has been directed to niobium nitride, since it can have T_C as high as 17.3 K [21]. The applications of NbN are wide, the material has been used as hard coatings [99], small scale Josephson junctions [A.I], [24, 26, 100], thermometers [A.II, A.III], bolometers [25, 101] and single photon detectors [102].

Unfortunately, the NbN_x phase diagram is very complex as the NbN_x system crystallizes into various phases with fairly different properties [98, 103]. According to some published works [21, 104] stable NbN_x phases are: (i) α-NbN, with body

centred cubic structure (bcc), where nitrogen is embedded interstitially with x $<$ 0.40, (ii) β-Nb_2N with x $= 0.40 - 0.50$, (iii) γ-Nb_4N_3 with x $= 0.75 - 0.80$, (iv) δ-NbN with x $= 0.88 - 0.98$ and x $= 1.015 - 1.062$, (v) ϵ-NbN with x $= 0.92 - 1.00$, and finally also Nb_5N_6, Nb_4N_5 and Nb_3N_4 .

The properties of NbN_x system are very delicate to deposition conditions [A.II], [21, 38]. Even within the same crystal structure but different lattice spacing the critical temperature can vary significantly [A.II], [38]. Table 4.1 presents the highest critical temperatures typically achieved for the various NbN_x phases [21, 104–106], out of which the B1 (rocksalt) and simple cubic structures have highest T_C.

Niobium nitride films have been grown using numerous methods, for example reactive rf magnetron sputtering [95], chemical vapor deposition [107], ion beam deposition [108] and pulsed laser deposition [A.I, A.II, A.III], [38,104,109]. However, it should be stressed that the superconducting properties of NbN_x system are especially sensitive to the ambient nitrogen gas pressure, as well substrate material and temperature during deposition. All things considered, thin film deposition of NbN is far from trivial. NbN (simple cubic) phase has been observed only in films deposited by pulsed laser [22, 38, 104]. In addition, Nb_3N_4 exhibits superconductivity $\sim$6.7 K, but it is not studied well [22, 104]. Other observed, but even less studied, stable and unstable phases include ζ- and η-NbN [21, 98, 103, 110].

TABLE 4.1 Highest critical temperatures (T_C) typically achieved for the best studied NbN_x phases. Adapted from Ref. [21, 104–106]. In our films we have observed δ-NbN phase.

Compound	Critical temperature T_C (K)	Crystal structure
α-NbN	$< 4 - 9.2$	bcc
β-Nb_2N	$< 1.2 - 9.5$	hexagonal
γ-Nb_4N_3	$\sim 7.8 - 15$	tetragonal
δ-NbN	$\sim 9.7 - 17.3$	cubic B1 (rocksalt)
δ'-NbN	~ 7.2	tetragonal
(sc) NbN	~ 16.4	simple cubic
ϵ-NbN	< 1.2	hexagonal
Nb_5N_6	< 1.77	hexagonal
Nb_4N_5	$\sim 8.0 - 8.5$	tetragonal

4.1.2 Oxides of NbN

A drawback of this complex, but impressive material is the oxidation of the surface upon exposure to atmosphere. The oxide layer that forms on the topmost surface of NbN is Nb_2O_5, followed deeper by insulating $Nb_2N_xO_{5-x}$ ($x \leq 2$), and metallic interface oxide $Nb_{1-x}O_x$ ($x \leq 0.5$). The mean value of the thickness for the oxide saturation is 1.5 nm. Oxinitrides extend more than 2 nm deep into NbN serrating and segregating the NbN surface and deteriorating superconducting properties [111, 112].

4.1.3 TaN

Tantalum nitride (TaN) exhibits several different phases with different crystal structures and compound characteristics, just like NbN [98,113]. Similar to NbN_x system, TaN_x exhibits superconductivity and metallic properties depending on crystal structure. TaN has been used, for example, as high resistivity barrier layers in junctions [A.I], diffusion barriers [114] and superconductors [115] exhibiting $T_C \sim 8.2$ K.

4.2 Pulsed laser deposition and properties of NbN

NbN thin films with various thicknesses were deposited by pulsed laser ablation technique on 0.5 mm thick single crystals of magnesium oxide (MgO) substrates, with crystal orientation (100) and purchased from Crystec Gmbh. A Nd:YAG laser (EKSPLA Model: NL301 HT) produced ablating pulses of width 4 ns and wavelength of 1064 nm. Ablation of high purity niobium target was done in an N_2 gas atmosphere. The incident energy density was $\sim$6 J cm^{-2}. The deposition was performed in a base vacuum of $\sim 4 \times 10^{-6}$ Torr, in an all stainless steel vacuum chamber equipped with a dry mechanical and a turbomolecular pump. All the films were deposited at 600°C, known from earlier study [38] to be ideal for the growth of top quality superconducting films with high T_C and epitaxial structure. The atomic ratios of Nb and N in the films were varied by adjusting the nitrogen gas pressure in the deposition chamber. After the deposition at 600°C, the films were slowly cooled down to room temperature in a high vacuum.

An atomic force microscope was used for surface topography examination of the epitaxially grown 100 nm thick NbN film. A room temperature atomic force micrograph of the scanned area (5 μm $\times$ 5 μm) is shown in Fig. 4.1. The film presented a fairly smooth surface, with a root mean square surface roughness of $\sim$3 nm. Scanning electron microscope was used to scan larger areas of the film and to study particulate density, which was revealed to be very low. A reasonably smooth surface is essential for clean interfaces in superconducting devices and applications.

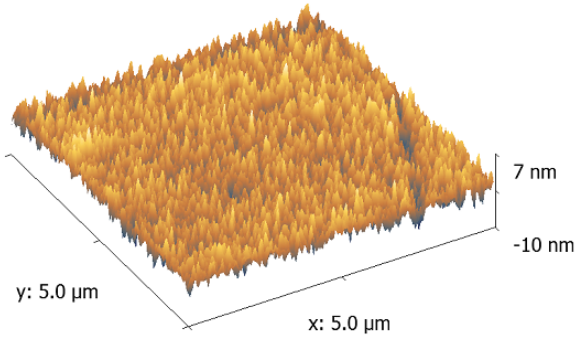

FIGURE 4.1 An atomic force microscopy scan of an NbN surface at room temperature. The film was epitaxially grown on (100) MgO with pulsed laser deposition. Figure adapted from Ref. [A.II].

The crystalline structures of the NbN thin films deposited on (100) MgO at 600°C at different nitrogen base pressures were studied with a X-ray diffractometer. Measured diffractograms are shown in Fig. 4.2.

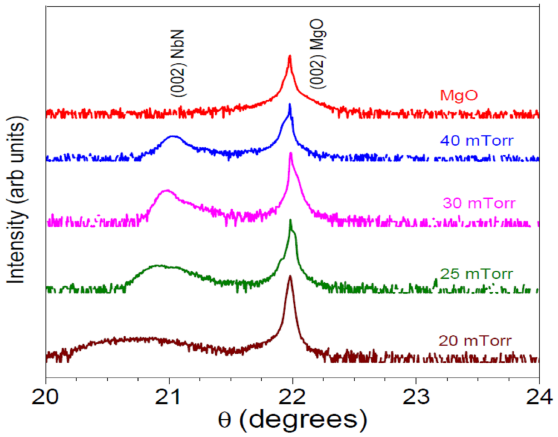

FIGURE 4.2 An X-ray diffraction patterns of NbN thin films deposited with various nitrogen pressures. The thickness of the films was 100 nm and (100) MgO was used as the substrate. The deposition temperature was 600°C for all samples. The intensity is presented in logarithmic scale. Figure adapted from Ref. [A.II].

The strong (002) reflection of MgO dominates the diffractograms, but on the left of the (002) MgO peaks a reflection of NbN emerges, especially for NbN grown between pressures 25-40 mTorr. The clear signature of the (002) direction indicates an epitaxial growth of the NbN film. The absence of the odd (00h) reflections in the diffraction pattern denotes that the crystal structure of the studied NbN film is face centred cubic (fcc). Previous results [22, 109, 116] have revealed a simple cubic structure of superconducting NbN fabricated on MgO by PLD, which is in contrast

to results in Ref. [A.II]. Nevertheless, PLD deposited superconducting films with the fcc phase have been observed previously. In reference [38] the out of plane NbN lattice parameter is smaller than the MgO lattice parameter, which is opposite to the results in Fig. 4.2. Figure 4.2 shows that the full width half maximum (FWHM) of the NbN diffraction peak and the out of the plane lattice parameter decreases with increasing N_2 pressure. Crystal structures of fcc and simple cubic NbN are shown in Fig. 4.3.

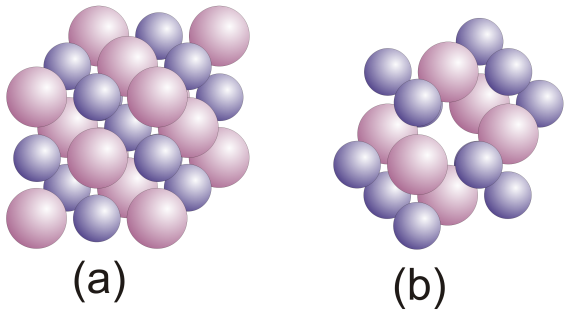

FIGURE 4.3 The schematics of (a) face centered cubic (fcc) rocksalt and (b) simple primary cubic (sc) crystal structures.

The dependence of T_C on N_2 base pressure of a 100 nm thick NbN film is presented in Fig. 4.4(a), which reveals that T_C is an extremely sensitive function of the nitrogen gas pressure during film growth (left slope ~0.6 K/mTorr and right slope ~1.6 K/mTorr). The highest critical temperature (~15.5 K) was obtained at the temperature of 600°C and 23.7 mTorr N_2 pressure (Fig. 4.4(b)). The resistivity of the film from room temperature to all way down to T_C was ~100 $\mu\Omega$ cm within accuracy of few percents.

As shown in figures 4.2 and 4.4(a), for N_2 pressures between 25-40 mTorr, the FWHM of the NbN diffraction peak decreases with increasing N_2 pressure, suggesting improved crystal quality. However, at the same time the out of the plane lattice parameter decreases and so does T_C. This implies that the changing nitrogen concentration inside the NbN crystal leads to a change in lattice dimensions. A change of the crystal dimensions results in an alteration of the phonon spectrum. This variation affects the superconductivity in NbN as a result of electron-phonon coupling.

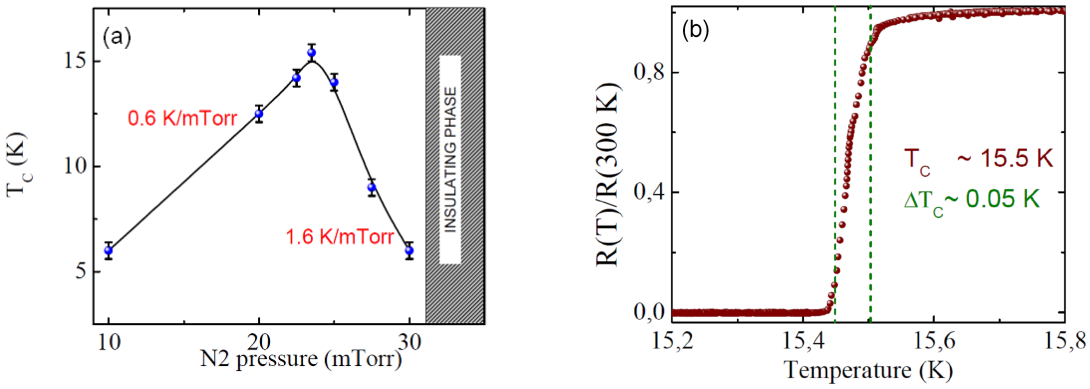

FIGURE 4.4 (a) The variation of the transition temperature (T_C) of NbN films with N_2 pressure. The films were deposited at 600 °C on (100) MgO. Interestingly, films ablated above 30 mTorr showed insulating properties. (b) The temperature dependence of resistance of the NbN film deposited on (100) MgO at 23.7 mTorr N_2 pressure and 600 °C revealing T_C ∼15.5 K. Width of the transition was ∼50 mK. Figures adapted from Ref. [A.II].

4.2.1 The fabrication details of Cu/AlO_x-Al/NbN and Cu/NbO_x/NbN based tunnel junctions

An NbN thin film, with a thickness of 30 nm, was grown on a MgO substrate with pulsed laser deposition using the fundamental 1064 nm laser pulse emission from Nd:YAG laser. The NbN films were deposited at 600°C and 23.7 mTorr of ambient nitrogen gas pressure, as these conditions were observed to be optimal for achieving high T_C NbN samples from Fig. 4.4(a). The temperature dependence of the resistance of the film is shown in Fig. 4.5 revealing $T_C \sim 10.8$ K along with a scanning electron microscope image of a Cu/AlO_x-Al/NbN based NIS junction with artificial colors. The lower T_C compared to the Fig. 4.4 films probably originates from pressure fluctuations during the deposition and/or reduced film thickness.

After the NbN ablation, a layer of PMMA resist diluted with anisole (CH_3O-C_6H_5) was used as an etch mask to make bond pads and base electrodes of the NIS junctions. The patterned areas of NbN were removed down to MgO by reactive ion etching, using a mixture of trifluoromethane CHF_3 (50 sccm) and oxygen O_2 (5 sccm) [117], using 100 W power at 55 mTorr pressure. The etching rate was ∼ 4 nm/min. Two ∼ 1 μm wide NbN electrodes were obtained along with pads and alignment marks which were close to the junction area. The separation between the NbN electrodes was ∼20 μm. The schematic steps of the fabrication are illustrated in Fig. 4.6.

In the next step, a dual layer of positive resist was used for the lithography. For

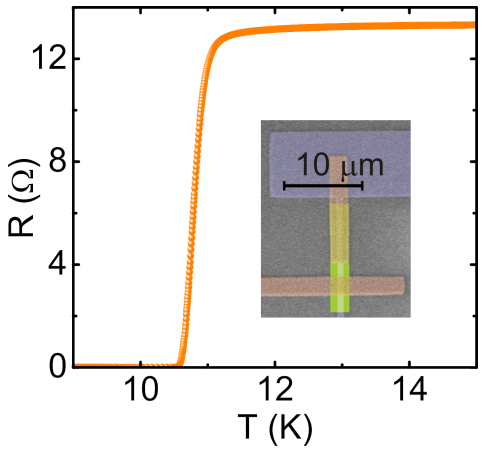

FIGURE 4.5 The temperature dependence of the resistance of 30 nm NbN deposited at 600°C and at 23.7 mTorr ambient nitrogen gas pressure. The inset shows an artificially color coded SEM image of the sample. NbN, Al and Cu are represented with violet, orange and green colors, respectively. The normal metal Cu island has a size of 38.5 μm $\times$ 2 μm $\times$ 80 nm. Figure adapted from Ref. [A.III].

the co-polymer layer commercially available P(MMA–MAA) resist diluted in ethyl lactate was used, while the top layer resist was PMMA diluted with anisole. Using alignment marks etched on NbN, the overlay was aligned to pattern the Al and Cu on top of the NbN base electrodes.

To get rid of organic impurities, the sample was cleaned in oxygen plasma for 30 seconds using reactive ion etcher before Al and Cu deposition. The metal evaporation was performed in an ultra high vacuum chamber. First 40 nm of Al was evaporated from an angle of 20 degrees with respect to the plane of the substrate (Fig. 4.6(c)), forming an Al coverage on top of NbN. This was followed by the oxidation of Al surface *in situ* for 4 minutes in 50 mbar O_2 pressure. Finally, 80 nm of copper was evaporated from the normal angle, depicted in Fig. 4.6(d). The chamber pressure during metal deposition was 2×10^{-8} mbar, and the evaporation rates for both Al and Cu were typically 0.1 nm/s.

After lift-off, the substrate was covered again with PMMA resist, and metal parts used for grounding were removed, using reactive ion etching of NbN. The grounding connections were necessary to avoid charging during EBL patterning. The charging effects can also be avoided by using a thin metal layer on top of or between the dual layer resists.

In addition to devices with AlO_x barriers, NbN/NbO_x/Cu/NbO_x/NbN SINIS junctions were also fabricated from 30 nm thick NbN. The sample fabrication process was almost similar to the NbN/Al-AlO_x/Cu/AlO_x-Al/NbN junctions, except that no Al was used in the former case. Instead, after the overlay patterning, sputter-

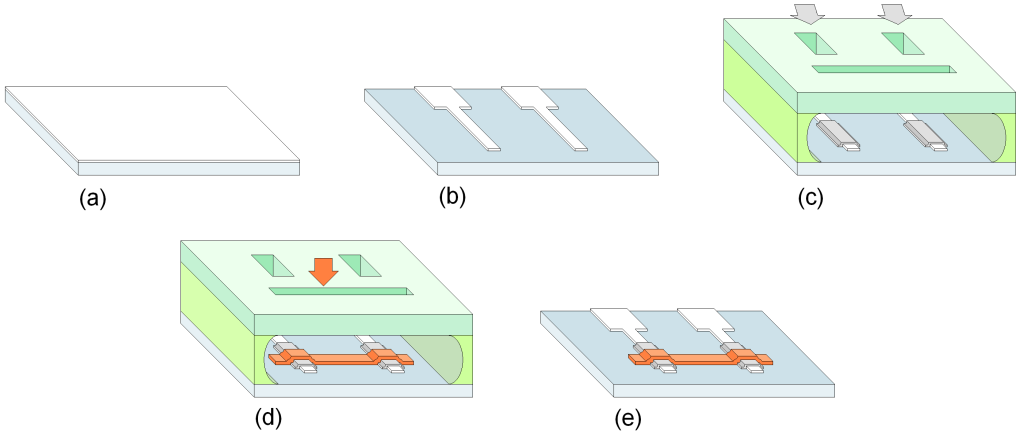

FIGURE 4.6 A schematic of the different steps involved in the fabrication of Cu/AlO_x-Al/NbN based tunnel junction. (a) A thin film of NbN on top of MgO. (b) NbN electrodes etched. (c) A double resist overlay and angle evaporation of Al followed by oxidation. (d) The evaporation of Cu from normal angle. (e) The final NbN based SINIS device.

ing with Ar-ions was carried out to clean the NbN surface at the junction area using thin Al as mask. The surface of NbN was then oxidized for 45 min in 350 mbar of O_2 pressure. Finally 40 nm of Cu was deposited to form the SINIS junction.

4.2.2 Fabrication of SNS Josephson junctions

The SNS Josephson junction trilayers (NbN/TaN/NbN) were fabricated on single crystal (100) MgO substrates (purchased from Crystec Gmbh) by pulsed laser ablation using a KrF excimer laser ($\lambda = 248$ nm) at IIT Kanpur. High purity niobium and tantalum targets in a multi-target carousel were ablated *in situ*, in a high purity nitrogen (N_2) environment [A.I]. Keeping laser pulse energy fixed at ∼145 mJ and optimizing the size of a laser spot on target and target-to-substrate distance, deposition rates of ∼0.4 nm/s for the NbN and ∼0.5 nm/s for TaN were achieved. The substrate temperature was 600°C for both NbN and TaN layer deposition. The deposition of NbN was always done at 80 mTorr N_2 pressure while TaN was grown at 70, 80 or 90 mTorr N_2 pressures in different runs. NbN layer on the top and base of trilayer had thickness of 200 nm while TaN in between was ∼10 nm thick.

The main reasons to choose TaN as barrier material were the tunability of TaN resistivity by varying growth conditions (e.g. pressure), and its observed high resistivity [23,26,118]. High resistivity results in higher resistance, and therefore possibly higher $I_C R_N$ products. Typical normal metals like Cu have too low resistivity values for SNS applications [23, 119]. Another reason was that the thermal, chemical

and mechanical properties of TaN are quite similar to NbN [98]. The main reason for NbN being a good choice was its high transition temperature (up to ∼17.3 K) enabling measurement and future applications at liquid ^{4}He temperature 4.2 K.

A set of NbN/TaN/NbN trilayer films, with TaN layer grown at three different N_2 pressures, were pattered by e-beam lithography as squares of sizes from 2.4 μm $\times$ 2.4 μm to 8 μm $\times$ 8 μm. In Fig. 4.7, schematic illustrations of the fabrication steps are presented.

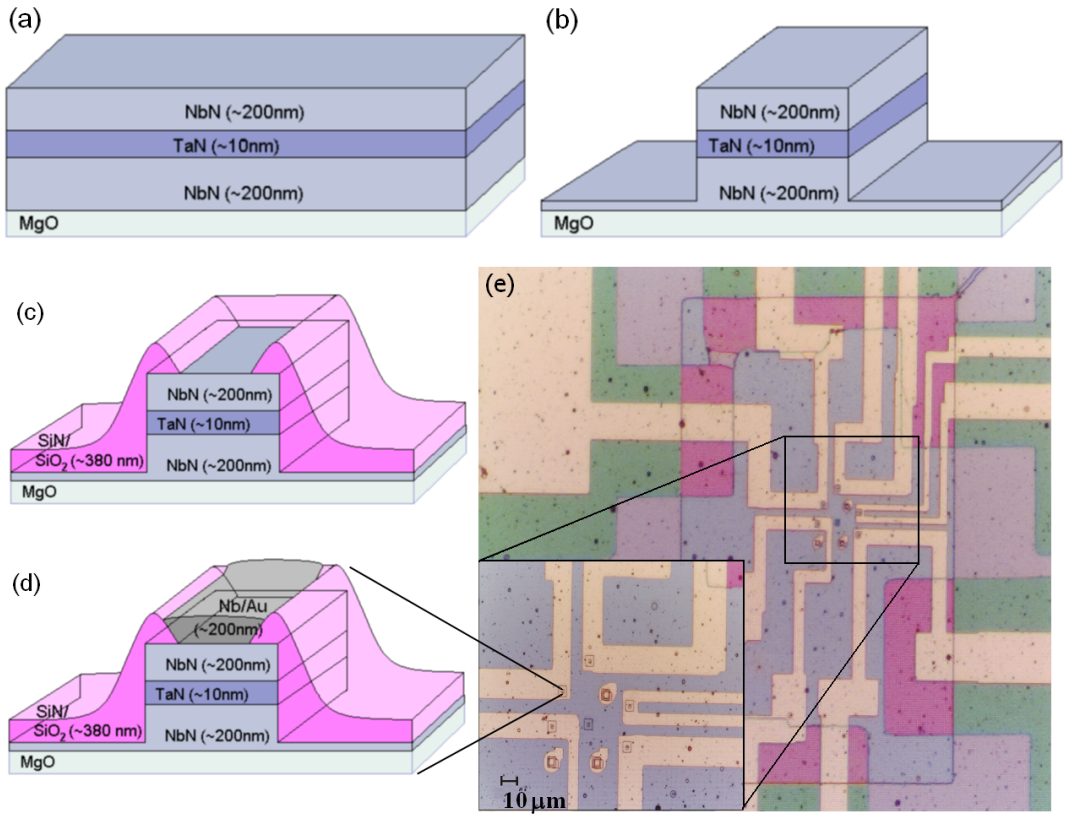

FIGURE 4.7 A schematic cross sectional view of the fabrication steps of the SNS device. (a) The NbN/TaN/NbN trilayer was grown by pulsed laser deposition on single crystal (100) MgO. (b) The device was patterned by e-beam lithography as squares and reactive ion etched to form the electrodes of SNS junction. (c) The growth of the highly aligned insulator (SiO_2 or Si_3N_4) was performed by PECVD. (d) The top contact metal (Nb or Au) layer was e-beam evaporated in an UHV chamber after the NbN surface was sputtered. (e) An optical microscope image of the device with a magnified view of the junction area as inset.

Reactive ion etching was carried out with a mixture of CHF_3 (75 sccm) and O_2 (5 sccm), and square shaped SNS pillars were etched out of the trilayers. During the reactive ion etching, the active device area was protected with an etch mask, a thin layer of aluminium between two resist layers, which was patterned and developed.

The rate for etching was ∼10 nm/min at 55 mTorr pressure and 150 W power. The height of the etched pillars were checked with an atomic force microscope (AFM) to confirm the etching rate. In addition, the lateral size was first verified with AFM, later with SEM.

An insulating layer (∼380 nm) silicon dioxide or silicon nitride was grown on the top of the device using PECVD. Before the insulating layer was grown, the surface was cleaned with gentle N_2 plasma etch. The insulators were deposited in two distinct steps: first at 150°C for a small region around the junction, and then at 300°C for the region below the bond pads. Both steps were followed by a lift-off. These two separate steps were necessary because, on one hand the SiO_2 or SiN growth at 300°C ensured enough mechanical strength to withstand bonding, while on the other hand an accurate small scale lift-off of SiO_2 or SiN was only possible for the insulator grown at 150°C. In addition, 150°C is around the maximum temperature that could be used to avoid the burning of the thinner conventional e-beam resists around the active device area.

The overlay e-beam lithography was used for patterning the top Nb or Au contacts. The evaporation rate for Nb or Au were 0.2 nm/s and 0.1 nm/s, respectively, and the evaporation was done in an UHV chamber. Before the deposition of a metal, a short and gentle O_2 plasma cleaning with RIE was applied to remove impurities, and 1 kV Ar-ion sputtering was performed *in situ* just before evaporation, to remove a possible thin oxide layer on the NbN surface. Ar-ion sputter cleaning has been shown to be a useful tool to reduce the NbN surface contact resistance [101], and we also observed that Ar-sputtering was necessary to make a good quality contact between the top NbN layer and Nb or Au metal. The other contact on the bottom NbN electrode was a direct bond far from the device area.

4.2.3 Fabrication of NbN samples for magneto-optical imaging

For the magneto-optical imaging work [A.V, A.VI] research, NbN was grown on (100) MgO with excimer laser using similar parameters as NbN deposited for SNS Josephson junctions. The thickness of the NbN films was 280 nm. Several rectangular NbN windows (size ∼2.4 mm × 4.8 mm) were processed by reactive ion etching using a mixture of CHF_3 and O_2, using a layer of PMMA and a thin layer of Al as an etch mask. E-beam lithography ensured NbN rectangles with very smooth edges, necessary for flux penetration studies with magneto-optical imaging.

4.2.4 Fabrication of Cu/AlO_x-Al/Nb based tunnel junctions

In Fig. 4.8(a), the SEM image of the Cu/AlO_x-Al/Nb based double NIS junction is shown. The device comprises of two large outer junctions and four smaller inner junctions. A closeup of one of the smaller junction is shown in Fig. 4.8(b). The tapering Nb electrode and Al coverage of the Nb electrode are clearly visible. The schematics of the fabrication steps are shown in Fig. 4.8(c)-(f).

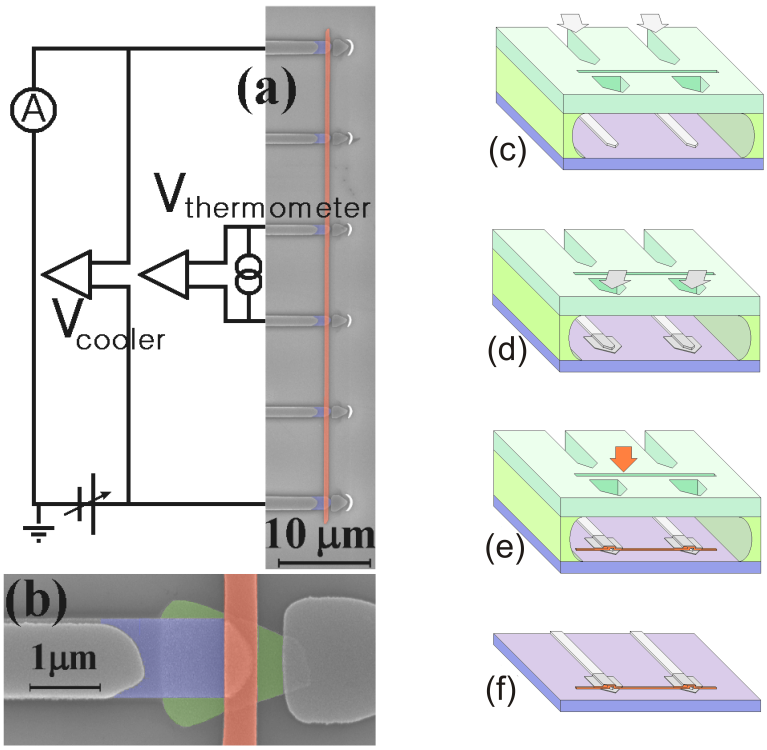

FIGURE 4.8 (a) An artificially coloured image of the device taken with a SEM alongside the bias configuration. A pair of inner electrodes operates as a thermometer to measure the electron temperature of the Cu wire while the outermost electrodes acts as the cooler junctions. (b) A high resolution SEM image of a single NIS junction showing the tapered Nb (blue) tip covered with Al (green) on the junction area, contacting the Cu (red). Right: Schematics of the steps involved in the fabrication of Nb/Al-AlO_x/Cu/AlO_x-Al/Nb based junction: (c) angle evaporation of Nb followed by Al is evaporation from the same angle. (d) The half of the total Al evaporated from opposite angle followed by oxidation with O_2. (e) Evaporation of Cu from normal angle. (f) Cu/AlO_x-Al/Nb based SINIS device. Figures (a) and (b) adapted from Ref. [A.IV].

Starting with a thermally oxidized silicon substrate, a double layer of positive resists was used for the e-beam lithography. The commercially available resists for the bottom co-polymer layer was P(MMA–MAA) diluted in acetic acid (CH_3COOH), while the top layer resist was PMMA diluted in anisole. The thick-

nesses of the individual resist layers were ∼500 nm (bottom) and ∼450 nm (top) with baking times were 15 and 5 minutes, respectively, at a temperature of 170°C. The double resist layer was then e-beam exposed and subsequently developed forming an undercut structure partly resembling a hanging bridge. The sample was then cleaned in an oxygen plasma for 30 seconds using a reactive ion etcher to get rid of organic impurities, and after that the metals were evaporated in an ultra high vacuum chamber.

For the first evaporation step, 20 nm of Nb was evaporated from an angle of 30 degrees with respect to the plane of the substrate at a rate of ∼0.45 nm/s, as depicted in Fig. 4.8(c). After the evaporation of Nb, a quarter of an hour was waited, since cooling of Nb after the deposition has been shown to improve the quality of Nb based junctions [15].

In the next step, Al was evaporated at the rate of ∼0.1 nm/s on the top of Nb metal. One half of the total Al to be deposited was evaporated from the same 30 degree angle as Nb, while the other half was deposited from -30 degrees, as shown in Fig. 4.8(d) To improve the Al coverage on top of Nb, the end of the the Nb electrode in the junction area was designed to be slightly tapering, as shown in Fig. 4.8(b). The idea behind tapering the Nb electrode tip and the Al deposition from two different angles was to ensure complete Al coverage on the top as well as on the edges of the Nb electrode, even with a thin layer of Al. After the Al evaporation, the Al surface was oxidized at 350 mbar of O_2 pressure for 25 minutes in situ. In the last step, 35-50 nm copper was evaporated at ∼0.1 nm/s from the normal angle on top of structure (Fig. 4.8(e)). The schematics of the final device after lift-off is presented in Fig. 4.8(f), and SEM micrographs in figures 4.8(a) and (b).

Three different SINIS junctions were fabricated. All had the same thickness (∼20 nm) of Nb, but the Al (Cu) thickness varied and were − 7 (35) nm, 10 (40) nm and 20 (50) nm. The Cu wire was ∼55 micrometers long and ∼400 nm wide.

For the Nb electrodes, the thickness 20 nm and line width (∼1 μm) were chosen so that Nb could still show T_C and Δ close to the bulk value, but also so that a thin film of Al would perfectly cover the Nb metal layer in the junction area. Previous studies with Nb films show that thickness, line width and deposition conditions during e-beam evaporation have a strong effect on T_C and Δ of Nb [9,13,17–19,120, 121].

Chapter 5

Experimental results

In this chapter, the experimental and some theoretical results of NbN and Nb based superconducting tunnel junctions are presented, in addition to studies of NbN/TaN/-NbN Josephson junctions.

5.1 Performance of the Cu/AlO_x-Al/Nb based tunnel junctions

First, the differential conductance-voltage ($\mathrm{d}I/\mathrm{d}V - V$) characteristics for Cu/AlO_x-Al/Nb double NIS junctions with three different thickness of Al (20 nm, 10 nm and 7 nm) were measured at bath temperature (T_{Bath}) of 150 mK. The results are shown in Fig. 5.1.

An overspill of Al on top of Nb assures a total coverage of the Nb edges. However, the overspill of Al should be minimized to ensure full lateral proximity effect. Alignment accuracy of a few nanometers is almost impossible to obtain with the resolution of EBL, thus a full lateral proximisation of the Al layer is very difficult to obtain. Hence it is possible and very likely that for this kind of junctions, part of the current in the device flows into the copper through the region where the Al is not fully proximised by Nb.

This situation can be approximated by a model where the Cu/AlO_x-Al/Nb tunnel junction can be thought to be made of two distinct junctions existing in parallel. The brief description of this model is: one of two parallel junctions, which has Nb electrode with Al-AlO_x/Cu on top of it, is named J_1. In junction J_1, Al is proximised by Nb in the direction that is perpendicular to the plane of the substrate, resulting in the superconducting gap value Δ_1. The second junction J_2 represents the overspilled Al with AlO_x/Cu on top of it. In this junction area, Al is proximised

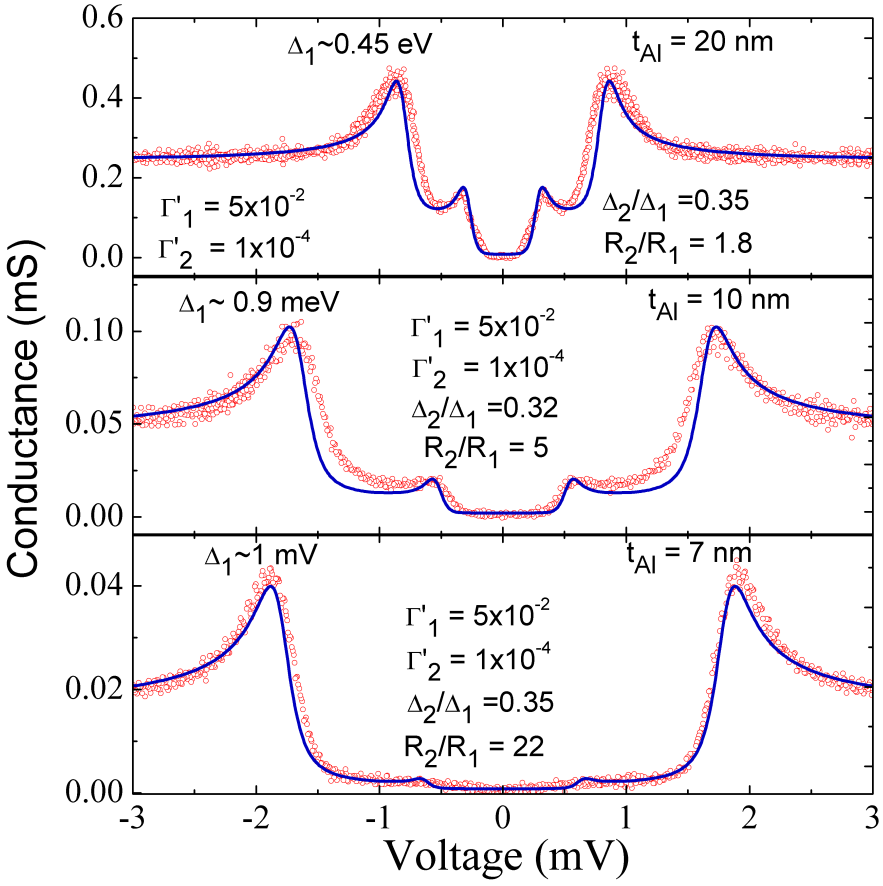

FIGURE 5.1 The measured differential conductance-voltage response of the Cu/AlO_x-Al/Nb based SINIS device with three different Al thickness 20 nm, 10 nm and 7 nm. The measurements were performed at a bath temperature of 150 mK and the measured data is indicated by red dots, whereas theoretical fits using a parallel junction model arising from Al overspill are presented by blue lines.

by Nb metal in the in-plane (lateral) direction of the substrate and the gap value of this junction is Δ_2.

The SINIS structure is comprised of two Cu/AlO_x-Al/Nb NIS junctions, which both are parallel combinations of J_1 and J_2. The total current I_{tot} through one Cu/-AlO_x-Al/Nb NIS junction is the sum of the currents tunneling through J_1 and J_2, thus $I_{tot} = I_{J_1} + I_{J_2}$. The total cooling or heating power of NIS device is the sum of the powers of J_1 and J_2 i.e. $\dot{Q}_{J_1} + \dot{Q}_{J_2}$.

In the framework of this model, the shape of the $\mathrm{d}I/\mathrm{d}V - V$ characteristics is determined by two parameters: (i) the ratio of gap values Δ_2/Δ_1 and (ii) the ratio of tunneling resistances of the junctions J_1 and J_2, R_2/R_1. This model was used to fit the theoretical curves in Fig. 5.1, using Dynes parameters $\Gamma'_1 = 5 \times 10^{-2}$ and $\Gamma'_2 = 1 \times 10^{-4}$ for the model.

The fitted theoretical curves show that the tunneling resistances of the two parallel junctions R_2 and R_1 are comparable with each other in the samples where the thickness of Al is 20 or 10 nm. These samples also had a larger lateral overspill of Al (200-300 nm) compared to sample with Al thickness of 7 nm, which had lateral overspill $<$ 100 nm due to better better alignment of Nb and Al layers. The lower gap is clearly suppressed in the device with Al thickness of 7 nm, as shown in Fig. 5.1. Reducing the Al overspill increases the resistance R_2, thus more current will flow through tunnel junction J_1.

However, even for the smallest obtained overspill Al full lateral proximisation of the Al layer was not accomplished, as shown in Fig. 5.1. With decreasing Al thickness (20, 10 and 7 nm), the degree of proximisation of Δ_1 increases gradually starting from $\sim$0.45 meV, then reaching $\sim$0.9 meV and finally achieving $\sim$1 meV, with Al thickness of 7 nm.

The sample with Al thickness of 7 nm showed $T_C \sim 6$ K, which is in approximate agreement with BCS superconducting energy gap equation (2.1). SINIS junctions with Al thickness of 5 nm were also made, but they exhibited leaky behaviour, suggesting that the coverage of Nb with Al was probably not continuous over Nb edges. More sophisticated methods will be needed to make such thin films continuous [33, 122]. One interesting and desired point about thin Al films, which should also be noted here, is that thin aluminium layers show an enhancement in the value of superconducting gap and T_C [33, 34, 123].

The devices with Al thickness of 7 nm was studied further. The dI/d$V - V$ and $I - V$ characteristics of the device at four different bath temperatures $T_{Bath} = 150$ mK, 500 mK, 900 mK and 1200 mK are presented in Fig. 5.2. The conductance curve reveals the total device tunnelling resistance $R_{\mathcal{T}} \sim 60$ kΩ. For the sample under study, the electron gas volume (Ω) was ~ 55 μm $\times$ 400 nm $\times$ 35 nm $\sim 0.8\mu$m^2 and the coupling constant $A \sim 4 \times 10^5$. For Cu the exponent n = 5. These parameters are needed for calculation of normal metal electron temperature $T_{\mathrm{N},e}$ as a function of V and T_{Bath} using equation (2.31). Examples of calculated theoretical curves are presented in Fig. 5.2 for 150 mK and 1200mK, fitting the experimental data well. However, the magnitude of the subgap current is larger than in pure Al junctions the low bath temperatures and it increases with temperature. This excess subgap current may arise due to the larger Dynes parameter of Nb that leads to heating effects [6].

The thermometric response and the electronic cooling performance of the SINIS device was also studied. In Fig. 5.3(a), thermometer voltage versus bath temperature is shown for device with 7 nm Al thickness and bias current $I_{Bias} = 3.5$ nA. Thermometry characteristics for device with 10 nm Al thickness and $I_{Bias} = 20$

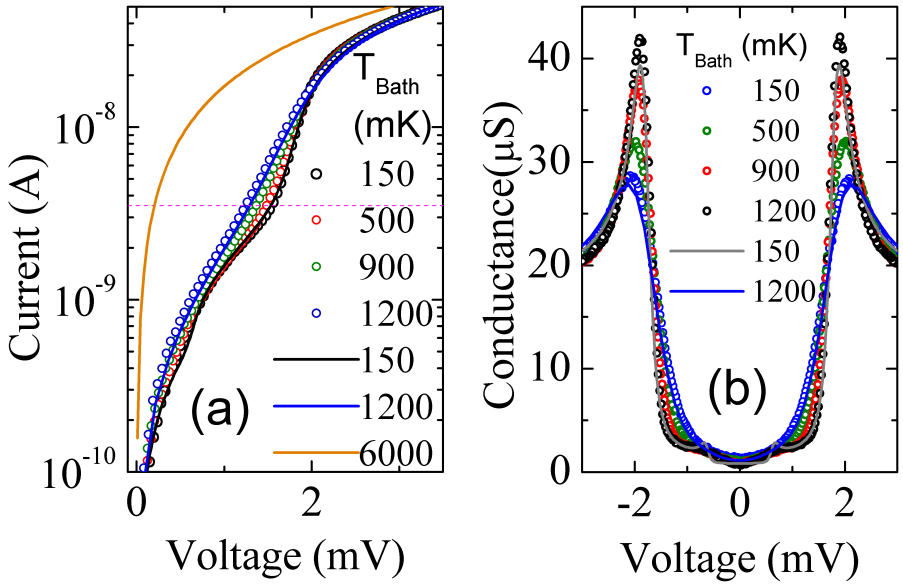

FIGURE 5.2 The current-voltage (a) and differential conductance-voltage (b) characteristics of Cu/AlO_x-Al/Nb based SINIS tunnel junction with Al thickness of 7 nm. The dots represent experimental measured data whereas solid lines are theoretical fits at bath temperatures of 150 mK, 1200 mK and 6 K (normal state). A constant current bias is presented in (a) as the dotted pink line. Figure adapted from Ref. [A.IV].

nA are presented in Fig. 5.3(b). In addition, theoretical fits with the assumption $T_e = T_{Bath}$ are also shown in figures 5.3(a) and 5.3(b). Measurements revealed a good thermometric sensitivity ∼0.2-0.3 mV/K from ∼200 mK to ∼5 K for the studied Cu/AlO_x-Al/Nb based SINIS junctions.

For the cooling experiment, the device with 7 nm Al coverage was studied. The sample had 6 junctions as seen in Fig. 4.8(a). The outermost junctions, used as cooler junction, were slightly bigger and their linewidth was about 1.3 micrometers. The two innermost smaller junctions were biased with constant current of 3.5 nA and they served as the thermometer. The voltage response of the thermometer as a function of the cooler bias was measured, while the bath temperature was kept constant. The bias configuration is also shown in Fig. 4.8(a). The variation of $T_{\mathrm{N},e}$ as a function of cooler voltage is shown in Fig. 5.3(c). In the subgap region and at the lowest bath temperatures, heating due to excess current dominates, but at higher values of T_{Bath} less heating is observed. It seems that, there is a competition between the subgap heating and the cooling, which emerges as a small dip in $T_{\mathrm{N},e}$ at values $V \sim 2\Delta_1$ where cooling dominates, especially with bath temperatures 500-700 mK.

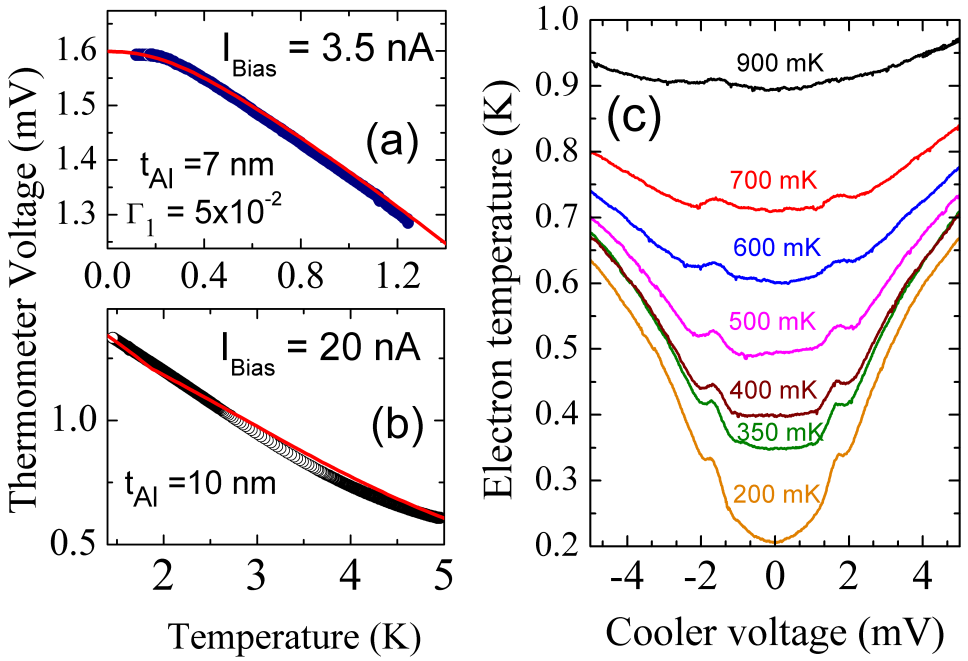

FIGURE 5.3 (a)The voltage drop across the thermometer junctions as a function of the temperature for devices with 7 nm Al with bias current 3.5 nA and (b) 10 nm Al with bias current 20 nA. The measured values are presented as dots and the corresponding theoretical fits as solid red lines. (c) Measured electron temperature of the normal metal (Cu) as a function of cooler voltage at seven different bath temperatures from 200 mK to 900 mK for device with Al thickness of 7 nm. Figure adapted from Ref. [A.IV].

5.2 Performance of the Cu/AlO$_x$-Al/NbN based tunnel junctions

The preliminary $I-V$ and dI/d$V-V$ measurements of NbN based junctions with AlOx barriers at 4.2 K [A.II] are shown in Fig. 5.4. The superconducting energy gap value 2Δ is observed to be $\sim$4 meV, which is reasonably close to the value of $\sim 5-6$ meV for high quality NbN [23]. The theoretical and measured differential conductance are also shown in the inset of Fig. 5.4. The value of tunneling resistance was about $\sim$300 kΩ.

Current-voltage characteristics for another device was taken at four different bath temperatures from 100 mK to 4.2 K and is shown in Fig. 5.5(a). The clear observation is that the tunneling resistance of the device is again fairly large $\sim$800 $k\Omega$. Such a large R_T value is a good feature for thermometry purposes, since self heating/cooling is small. However, the value of R_T is far too high for cooling appli-

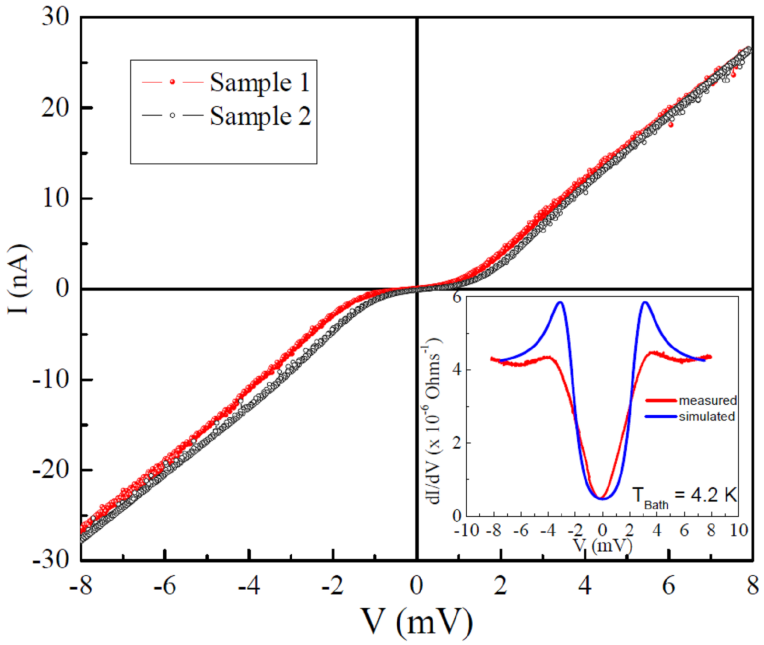

FIGURE 5.4 The measured current-voltage ($I-V$) characteristics of two different NbN based SINIS tunnel junctions at 4.2 K. The inset shows conductance-voltage curve for one of the junctions (red) with theoretical fit (blue). Figure adapted from Ref. [A.II].

cations, because the cooling power is inversely proportional to tunneling resistance $\dot{Q}_{\mathrm{NIS}} \propto 1/R_{\mathcal{T}}$.

The corresponding $\mathrm{d}I/\mathrm{d}V - V$ characteristics were also measured at four different temperatures from 100 mK to 4.2 K as well, and are shown in Fig. 5.5(b). The conductance curves revealed two distinct peaks near $V \sim 2$ mV. These two distinct peaks suggest that there are actually two tunnel junctions in parallel, junctions J_1 and J_2 – a case similar to and already discussed in context to Nb/Al-$\mathrm{AlO_x}$/Cu/$\mathrm{AlO_x}$-Al/Nb junctions. At 100 mK, the peak appearing at 2.1 mV is labelled J_1 while the other at 2.5 mV is labelled J_2. The position of the J_1 peak does not change with temperature, but the peak J_2 does. With increasing temperature, J_2 peak shifts towards J_1 and at the temperature 1200 mK J_2 merges with J_1.

It is speculated that the peak J_1 corresponds a Cu/$\mathrm{NbO_x}$/NbN junction as it is temperature independent and J_2 corresponds to an Al/$\mathrm{NbO_x}$/NbN and a Cu/$\mathrm{AlO_x}$/-Al junction in series. We suspect that there is always an insulating barrier between the base electrode NbN and Al or between NbN and Cu.

The hypothesis is, that the insulating barrier on top of NbN is the native $\mathrm{NbO_x}$, formed during lithography steps when the film is exposed to atmosphere [124, 125]. The Ar-ion sputtering *in situ* before the metal deposition has been shown to improve the junction characteristics [A.I]. However, the reason why Al layers do not work as

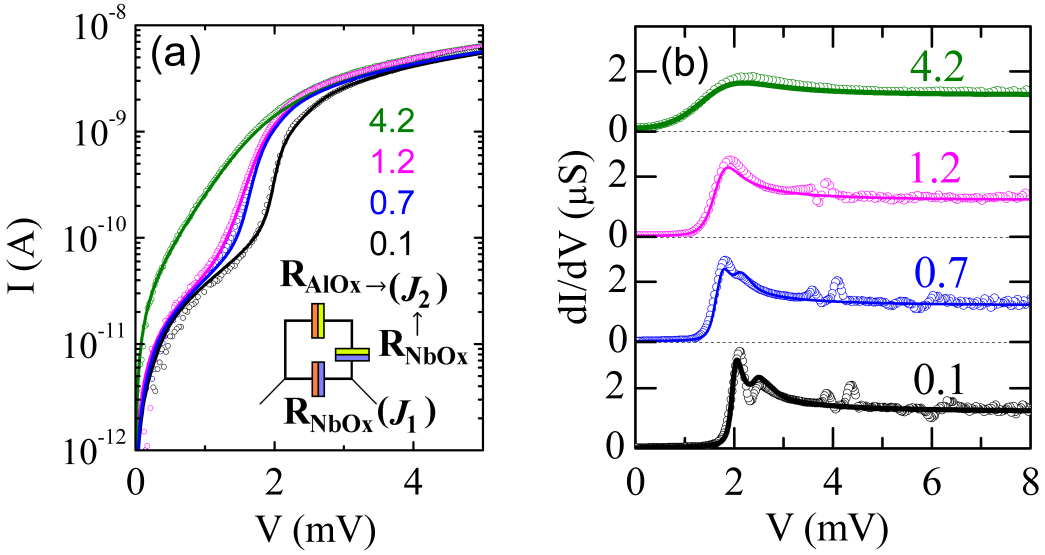

FIGURE 5.5 The temperature dependence of (a) current-voltage and (b) conductance voltage characteristics of a NbN based tunnel junction with corresponding theoretical fits at four different bath temperatures. The inset in (a) presents equivalent circuit schematics assuming a parallel junction network model. The experimental data is presented as dots while fits with lines corresponding to the theoretical results calculated with parallel junction network model. Figure adapted from Ref. [A.III].

well on top of NbN as on Nb has been speculated for example in Ref. [126]. It has been suggested that an extra barrier of aluminium nitride (AlN) is formed at the NbN-Al interface [126] due to the affinity of Al to absorb N atoms from the NbN surface, and leaving behind a disordered Nb layer at the interface. This situation does not rise in the case of Nb, since there is no nitrogen available. Consequently, an extra barrier layer (NbO_x or AlN) between the two superconductor NbN and Al will most likely form. Thus in this case instead of a simple NIS device, we have one NIS junction (J_1) and the $NI_1S_1I_2S_2$ type of junction (J_2).

A direct contact between NbN/NbO_x and Cu can originate due to an incomplete coverage of NbN at the edges, or due to particulates of the target material on the surface of NbN. Since particulates can be of various sizes, even 40 nm of Al may not cover them throughout. The conductance maxima of J_1 (2.1 mV at 100 mK) is identified with $2\Delta_{NbN}$. The maxima of J_2 occur at 2.5 mV at 100 mK and since the difference between the peaks is about $\sim$ 0.4 mV, J_2 is suspected to correspond $2\Delta_{NbN} + 2\Delta_{Al}$. Thus $\Delta_{Al} \sim 0.2$ meV, which is close to the superconducting gap value for typical Al film thickness of 40 nm. In addition, J_2 merges with J_1 at 1.2 K, which is critical temperature of Al with $\Delta_{Al} \sim 0$.

The conductance characteristics show that $\Delta_{NbN} \sim 1.0$ meV, which is consid-

erably smaller than the gap value ∼1.6 meV obtained from the BCS equation (2.1) with the measured $T_C = 10.8$ K. One possibility for the suppression of Δ_{NbN} is the formation of segregated Nb oxide clusters [111, 112] in NbN due to the exposure of the NbN surface to atmosphere, which was unavoidable during the sample fabrication process. Oxides of Nb are known to reduce Δ_{NbN} of NbN based junctions [127], and they can act as catalysts [128] favouring the formation of ϵ-NbN with reduced $T_C < 1.77$ [21]. Furthermore, the local superconducting gap value is affected by regional disorder in the film structure of NbN. These spatial variations of Δ_{NbN} have been observed [129].

The equivalent circuit schematic of the parallel junction network model is presented in the inset of Fig. 5.5(a). The current-voltage $I - V$ and differential conductance-voltage $\mathrm{d}I/\mathrm{d}V - V$ characteristics are shaped by two parameters (i) $\Delta_{\mathrm{Al}}/\Delta_{\mathrm{NbN}}$ and (ii) the tunneling resistances $R_{\mathcal{T}}$; of the three tunnel junctions barriers $\mathrm{NbO_x}$ of J_1, $\mathrm{AlO_x}$ and $\mathrm{NbO_x}$ of J_2. The theoretical fits in Fig. 5.5 were obtained using Dynes parameters $\Gamma'_{\mathrm{Al}} = 1.0 \times 10^{-4}$ and $\Gamma'_{\mathrm{NbN}} = 2.3 \times 10^{-2}$, following the experimental data fairly well. Also, the parallel junction network model gives a specific resistance for $\mathrm{NbO_x}$ ∼2 MΩ μm^2, which is quite close to reported value in Ref. [124]. Nevertheless, the specific resistance for $\mathrm{AlO_x}$ was found to be ∼1 MΩ μm^2, which is practically three orders of magnitude higher as compared to specific resistance of typical $\mathrm{AlO_x}$ junctions [39]. The origin of this high resistance is not yet clearly understood.

5.2.1 Performance of NbN/$\mathrm{NbO_x}$/Cu/$\mathrm{NbO_x}$/NbN junction at 4.2 K

The preliminary results for $\mathrm{NbN/NbO_x/Cu/NbO_x/NbN}$ junctions were measured at 4.2 K. The $I - V$ and $\mathrm{d}I/\mathrm{d}V - V$ characteristics are presented in Fig. 5.6. The critical temperature of this NbN film was ∼12.5 K, predicting a $2\Delta_{\mathrm{NbN}} \sim 3.8$ meV, but a reduced gap is observed from the $I - V$ characteristics again ($2\Delta \sim 2.5$ meV). The size of the junction was $\sim 0.5 \times 1.3$ μm^2 and $R_{\mathcal{T}} \approx 120$ kΩ.

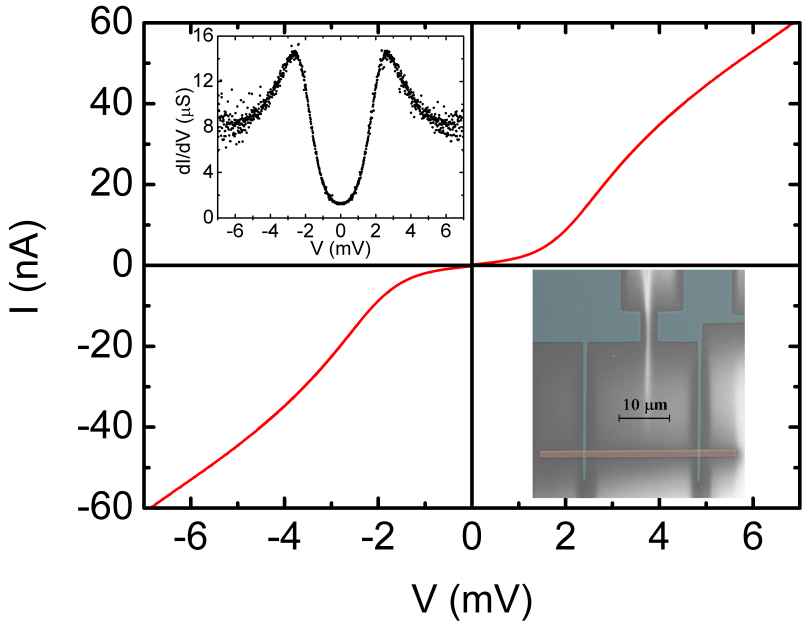

FIGURE 5.6 The current-voltage characteristics of the NbN/NbO_x/Cu/NbO_x/NbN junction at 4.2 K. The insets present conductance-voltage characteristics and SEM micrograph of the device with artificial colors, orange for Cu and blue for NbN.

5.3 Performance of the SNS Josephson junctions

In this section, first the performance of the junctions which has TaN layer grown at 80 mTorr, lateral sizes of 8 μm $\times$ 8 μm and Nb as the top contact are discussed. The typical variation of the junction resistance with temperature is presented in Fig. 5.7. High critical temperatures of NbN ($T_C \sim 15.7$ K) and Nb ($T_C \sim 8.8$ K) were observed, reflecting the high quality of the metallic films.

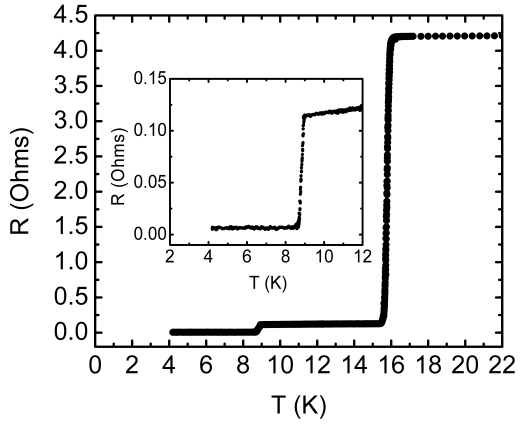

FIGURE 5.7 The resitance vs. temperature of an 8 μm $\times$ 8 μm NbN/TaN/NbN Josephson junction with an inset zoom-in of the Nb transition. Figure adapted from Ref. [A.I].

The $I-V$ characteristics of the junctions were measured at several different temperatures from 4.2 K to higher values. A set of curves for one sample is presented in Fig. 5.8(a), and for other sample (from 1.5 K to higher values) shown in Fig. 5.8(b). The junctions posses a large supercurrent branch. Noticeable rounding of $I-V$ characteristics at values around I_C in Fig. 5.8(a) is possibly due to thermal fluctuations [32]. However, other samples presented less pronounced rounding of the $I-V$ characteristics, but for example in Fig. 5.8(b), the critical currents of sample with the same lateral size are evidently lower compared to Fig. 5.8(a). This variation between two SNS devices (and others as well) is not properly understood at the moment, as relatively large differences were observed between individual SNS devices with the same lateral size, fabricated on the same substrate, in vicinity of each other, from nominally identical sandwiched NbN/TaN/NbN films.

The highest critical current value ~ 3.2 mA at 4.2 K in Fig. 5.8(a) is close to $I_C \sim 2.8$ mA at 1.5 K in Fig. 5.8(b), although same sample showed only $I_C \sim 1.2$ mA at 4.2 K. The $I-V$ characteristics also provided the R_{N} values. The R_{N} values were relative insensitive to temperature below $\sim$ 7 K for the ohmic region of the $I-V$

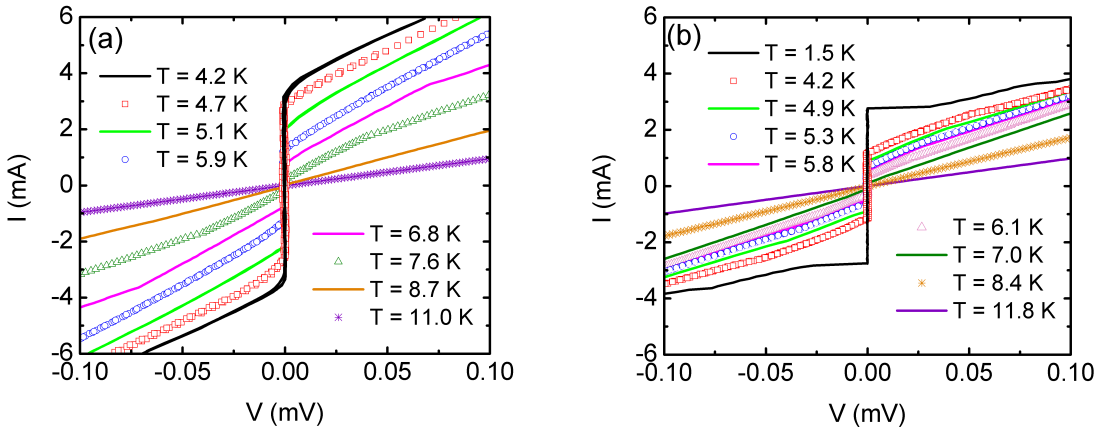

FIGURE 5.8 The current-voltage characteristics for two 8 μm $\times$ 8 μm NbN/TaN/NbN Josephson junction at different temperatures from (a) 4.2 K to 11.0 K, (b) 1.5 K to 11.8 K. Figure (a) adapted from Ref. [A.I].

curve. The highest R_{N} values observed were as high as 180 mΩ.

The samples whose $I-V$ characteristics is shown in Fig. 5.8(a) and (b) have resistances $R_{\mathrm{N}} \sim 25$ mΩ and ~ 42 mΩ, respectively. The Nb contact dominates the R_{N} values at ~ 11 K in Fig. 5.8(a)-(b) and Fig. 5.7, revealing a constant resistance $R_{\mathrm{N}} \sim$ 100 mΩ from all three plots. The $I_C R_{\mathrm{N}}$ values for four nominally identical 8 μm $\times$ 8 μm SNS junctions (fabricated from the same sandwiched trilayer with similar lateral size) were determined using the $I-V$ data, with the results for several different temperatures from 4.2 K to 8.7 K shown in Fig. 5.9. In addition, the inset shows the $I_C R_{\mathrm{N}}$ values of one 8 μm $\times$ 8 μm sample down to 1.5 K. The finite resistance of the Nb lead prohibited measurements above $\sim$9 K.

The theoretical predictions for $I_C R_{\mathrm{N}}$ values for different temperatures were calculated using Likharev's theoretical approximation, Eq. (2.22). First an estimation for the diffusion constant D in equation (2.20) is needed, and for that a reliable approximation for the TaN carrier density n is required. However, the carrier density n of TaN can vary a lot as a function of the TaN composition [130], therefore it is used instead as a fit parameter in the theoretical analysis. The resistivity of a 8 μm $\times$ 8 μm lateral size junction can be estimated from Fig. 5.8(a), by using the measured normal state resistance $R_{\mathrm{N}} \sim 25$ mΩ and the thickness of TaN layer ($L \sim 10$ nm), giving the resistivity $\sim$16 mΩ cm.

Furthermore, we fixed a value $2\Delta/(k_B T_C) \approx 4.0$ as observed for high quality NbN films [23,24] and used the measured $T_C \sim 15.7$ K. A carrier density $n = 1 \times 10^{21}$

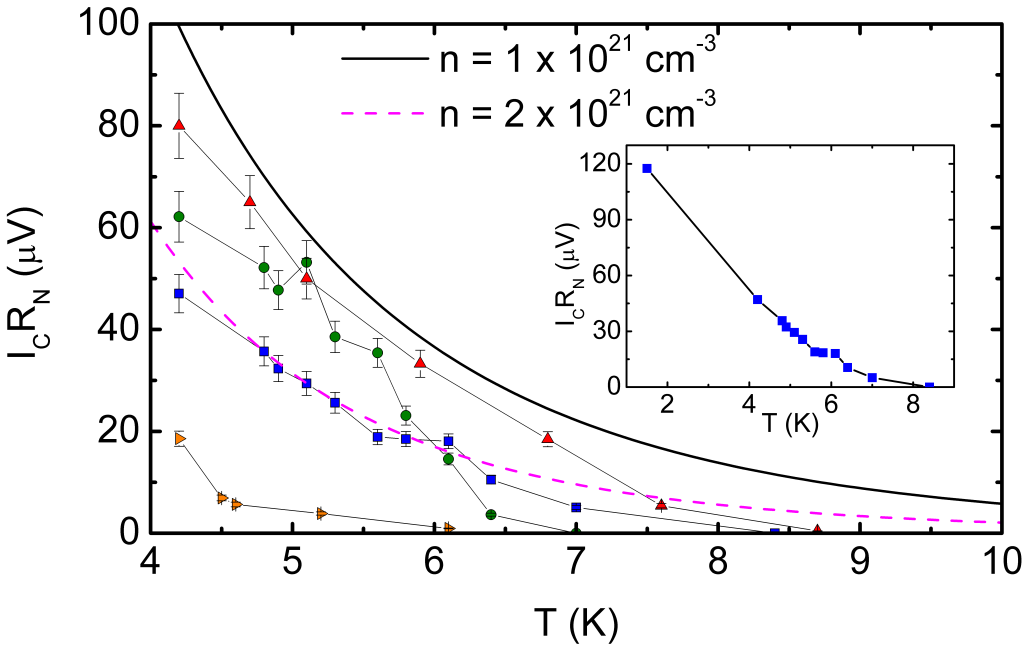

FIGURE 5.9 The temperature dependence of the $I_C \times R_N$ values (dots) obtained from $I - V$ characteristics for four distinct 8 μm $\times$ 8 μm junctions in addition to two theoretical curves correspond to different TaN carrier density n. The inset shows $I_C R_N$ values for a one junction from 1.5 K to 8.7 K. Figure adapted from Ref. [A.I].

cm^{-3} corresponds to a diffusion constant

$$D = \frac{1}{e^2 N_N(E_F)\rho} = \frac{1}{3}\frac{\hbar^2(3\pi^2)^{2/3}}{me^2\rho n^{1/3}} \approx 9.5 \times 10^{-6}\text{m}^2\text{s}^{-1},$$

where m and e are mass and charge of electron, respectively. The calculated $D \sim 9.5 \times 10^{-6}$m^{2}s^{-1} fulfills the condition $2\xi_N(T_C) \sim 2$ nm < 10 nm $= L$, so the range of validity in equation (2.22) is satisfied. The solid black curve in Fig. 5.9 represents the theory with the carrier density $n = 1\times10^{21}$ cm^{-3} as a parameter, and the dashed pink curve corresponds to the carrier density $n = 2\times10^{21}$ cm^{-3}, with $D \sim 7.5\times10^{-6}$m^{2}s^{-1}. The validity of equation (2.22) was also checked for this D, giving $2\xi_n(T_C) \sim 1.5$ nm < 10 nm $= L$. From Fig. 5.9 it is seen that the theoretical curves follow the measured values quite well. Nevertheless, one of the 8 μm $\times$ 8 μm devices showed clearly lower $I_C R_N$ values in Fig. 5.9, probably due to a bad quality Nb-NbN interface, or local quality problems in the NbN film induced by particulates. From the inset of Fig. 5.9 it is observed that the $I_C R_N$ value for one 8 μm $\times$ 8 μm is over two times

larger at 1.5 K than at 4.2 K.

Finally, the $I_C R_N$ values of several different junctions with different lateral sizes were studied. All of them had Nb contact electrodes and the same TaN thickness $L = 10$ nm, but varying TaN film resistivity, which was controlled by the nitrogen gas pressure during PLD deposition. Fig. 5.10 clearly shows that by increasing the pressure the $I_C R_N$ values increase. This pressure induced increase of the $I_C R_N$ is quite significant. However, it is caused due to an increase in I_C but not by R_N, which also depends the resistivity of TaN. Increasing resistivity of TaN as a function of increasing deposition pressure has been observed in Ref. [118]. Here, the smallest resistances $R_N \sim$ 2-15 mΩ were observed with the highest I_C values (with 2.4 μm $\times$ 2.4 μm), for TaN deposited at 90 mTorr. The highest $I_C R_N$ values at 4.2 K ($\sim$220-80 μV) are of the same order of magnitude as many previous studied NbN/TaN/NbN Josephson junctions devices [23, 26], but clearly less than the optimal results ($\sim$1-3 mV) in Ref. [23].

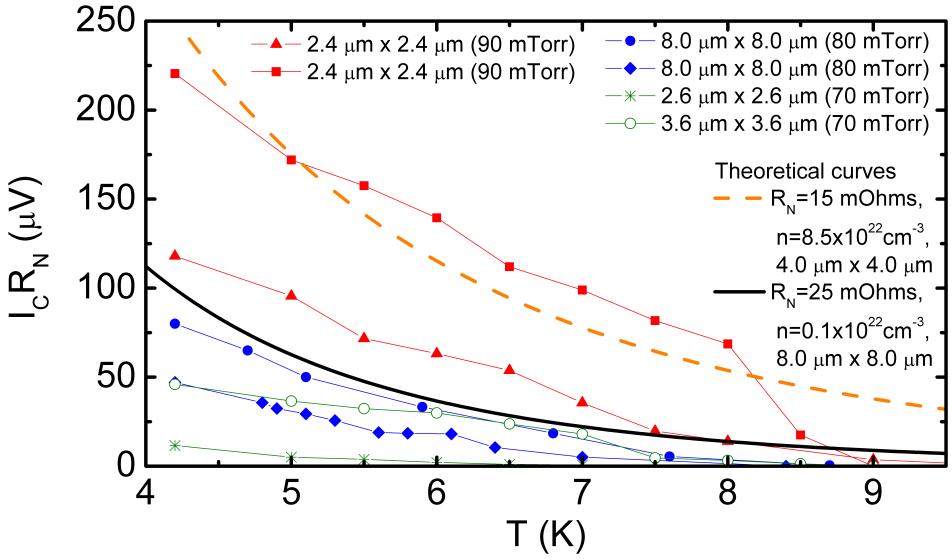

FIGURE 5.10 The temperature dependence of the $I_C \times R_N$ values (dots) obtained from $I - V$ characteristics for various sizes of junctions with TaN deposited at three different N_2 pressures. In addition, two theoretical curves with different TaN carrier densities n, normal state resistances and sizes of the junctions are presented.

An effect of the external magnetic field on the SNS Josephson junctions has also studied. The measurements were carried out at several different values of the magnetic flux densities from 0 T to 3.2 T at a temperature 4.2 K. The junctions were placed in a magnetic field so that the field lines penetrated the N layer along the

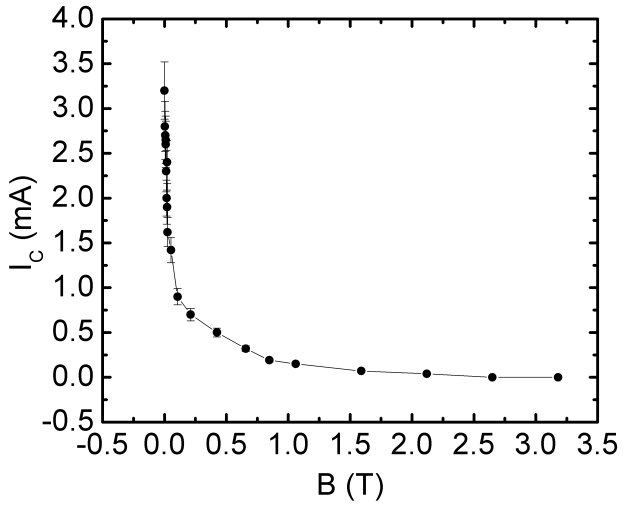

FIGURE 5.11 the critical current I_C vs. applied magnetic flux density B for a 8 μm $\times$ 8 μm NbN/TaN/NbN Josephson junction at the temperature of 4.2 K. Figure adapted from Ref. [A.I].

horizontal direction, i.e. 90 degrees with respect to the direction of the current flow through the junction.

A typical measured critical current vs. magnetic flux density (B) curve is presented in Fig. 5.11 for a 8 μm $\times$ 8 μm device. It did not show the simple Fraunhofer pattern of a clean and small Josephson junctions [2, 32], but with increasing B, the suppression of I_C to zero at 3 T was observed clearly. The fact that Fraunhofer pattern is absent in the $I_C - B$ characteristics is probably a result of a nonuniform critical current density at the junction area. The junctions with lateral dimensions (8 μm $\times$ 8 μm) were slightly larger than the Josephson penetration depth, estimated from equation (2.23) as $\lambda_J \sim 3$ μm.

Another clear observation was that the insulator material (SiO_2 or SIN) did not affect the electrical characteristics significantly. However, the usage of gold on top contact suppressed the supercurrent branch altogether, as seen in Fig. 5.12. This is presently not understood completely.

For more accurate characterization, we also applied the standard lock-in techniques to measure the four-probe differential resistance as a function of bias at different bath temperatures for both Nb and Au contact junctions. Results are presented in figures 5.13(a) and (b). The subharmonic gap structure in the differential resistance $\mathrm{d}V/\mathrm{d}I$ is complicated. Possible multiple Andreev reflections [131] inside the NbN superconducting gap do not match the expectation for high quality NbN, as

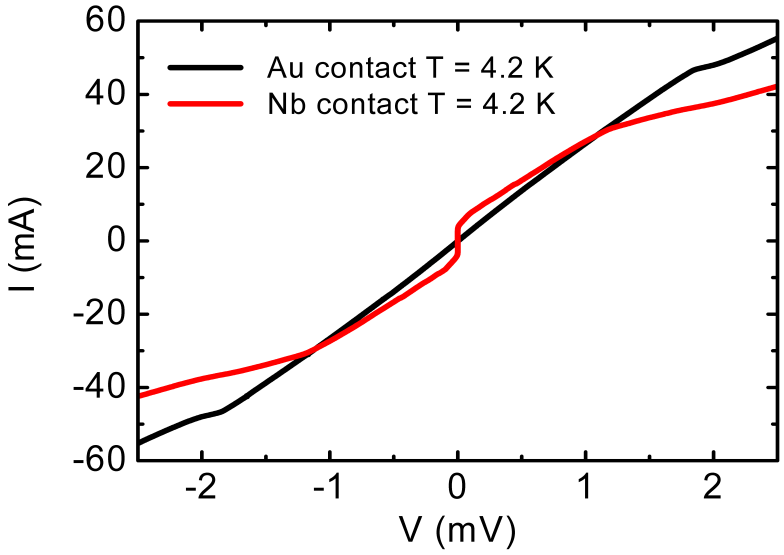

FIGURE 5.12 The current-voltage characteristics of two representative samples with Nb or Au contact electrode.

the temperature dependence of the voltage locations of the peaks or dips are already suppressed at $\sim$ 9 K. Thus, they do not follow the temperature dependent BCS superconducting energy gap function for NbN. The suppression of the supercurrent for the Au sample is clearly visible. There are also strong peaks in $\mathrm{d}V/\mathrm{d}I$ that move clearly with bath temperature. These peaks likely mark the point where Joule heating causes the top NbN electrode to turn normal. For the Nb contact electrode junction, the peak structure is more complicated, most likely because two different normal transitions take place: one for Nb at a lower bias and one for NbN at a higher bias. Once a part of the Nb electrode turns normal, the NbN is pushed more easily normal also due to increased power dissipation. The zero-bias resistance of the Au-sample cannot correspond to a series resistance of the Au film, as the observed value is much too high considering a typical Au film resistivity and the dimensions. It is possible that the interface quality between Au and NbN was not good enough.

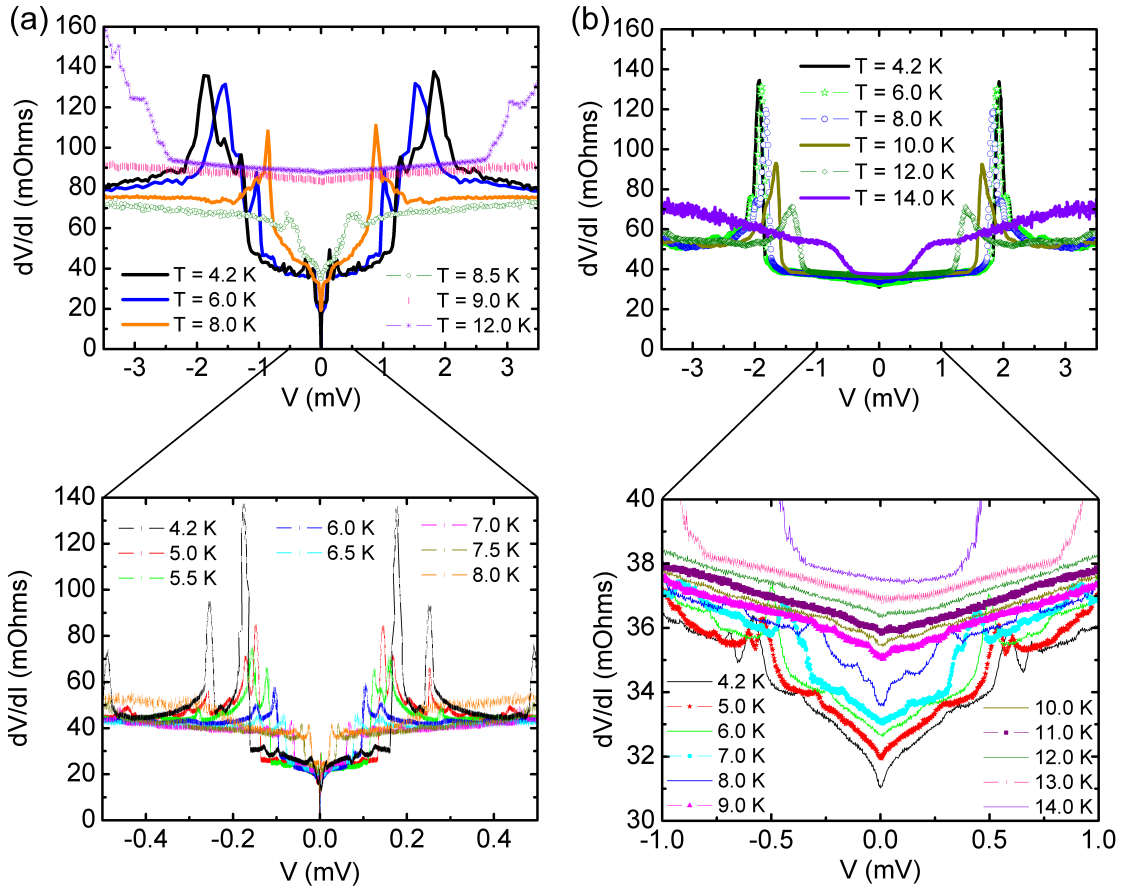

FIGURE 5.13 A differential resistance vs. voltage of a NbN/TaN/NbN Josephson junction with (a) Nb top electrode, (b) Au top electrode and zoom-ins of smaller voltage ranges.

Chapter 6

Conclusions

In conclusion, this thesis presents an approach towards the fabrication of normal metal-insulator-superconductor based junctions using superconductors with intermediate T_C. Practical realizations and further optimization of such devices will lead to the enhancement performance of the type of devices developed in this thesis.

Thermal multi-angle evaporation in an ultra high vacuum accompanied with conventional electron-beam lithographic techniques were used to successfully fabricate of Cu/AlO_x-Al/Nb based NIS tunnel junctions. Devices with different thicknesses of Al and varying amount of Al overspill over Nb were prepared. The best performance was found with the device with 7 nm thick Al and overspill less than 100 nm. A good thermometric response of Cu/AlO_x-Al/Nb based double junctions was observed between the temperatures of 200 mK and 5 K with responsivity $\sim$0.2-0.3 mV/K. In addition to thermometric response, the electronic cooling performance of the device was studied. At low temperatures and in the subgap region the heating associated with the excess subgap current were observed. The large Dynes parameter of Nb may give rise to such excess current. Nevertheless, small cooling effects were observed at bias voltages near the higher superconducting gap edge. Although electronic cooling below the bath temperature was not yet obtained, it is proposed that by increasing the cooler junction size and reducing the normal metal volume, cooling below the cryostat base temperature is possible.

In addition, high quality niobium nitride thin films were fabricated on (100)-oriented MgO with pulsed laser deposition using excimer and Nd:YAG based lasers. The high quality of the NbN films were reflected as high $T_C \sim 16$ K. The films deposited with Nd:YAG lasers had very low particulate density, hence the surface roughness was moderate, an essential feature for device application. The X-ray diffraction measurements revealed a fcc crystal structure, a commonly observed feature for superconducting NbN with high T_C. The transition temperature of NbN was found to be extremely sensitive to ambient gas pressure. A correlation between

lattice parameter, T_C and N_2 pressure emerged.

Pulsed laser deposition combined with conventional e-beam lithographic techniques was used to successfully fabricate Cu/AlO_x-Al/NbN and Cu/NbO_x/NbN tunnel junctions. The electrical properties of the junctions were investigated, and were found to be suitable for the thermometry purposes, as self heating effects were minimal due to the large tunneling resistance of NbO_x barrier. The conductivity studies at different temperatures suggested multiple barriers in the junction, including possibly a native surface oxide (NbO_x) of NbN formed upon exposure to atmosphere. The sufficiently low Dynes parameter ($\Gamma'_{\mathrm{NbN}} \sim 10^{-2}$) obtained from the theoretical fit using the multiple barrier network model is promising in the view of cooling applications, although the high value of tunneling resistance of the NbO_x barrier will limit the cooling performance. Also, even if natural NbO_x would be removed by sputtering, the layer of aluminium nitride (AlN) could form in the Al-NbN interface. For future projects, AlN might be an interesting barrier material for devices [100], since it can be grown *in situ* together with NbN by pulsed laser deposition.

High quality NbN/TaN/NbN trilayer films were also grown with pulsed laser deposition. The ambient gas pressure was varied causing a variation to the TaN layer resistivity. The NbN/TaN/NbN trilayer films were processed into square shaped Josephson junctions with different dimensions, smallest being 2.4×2.4 μm^2. An unconventional e-beam lithography-based technique that employed PECVD-grown SiO_2 and SiN insulator layers and their lift-off was developed to produce high alignment accuracy for the insulating layers in junction areas. It is possible to apply this method for a material friendly fabrication of closely packed submicrometer devices. The quality of the junctions were improved significantly by removing the native NbO_x and contaminants from the NbN surface by *in situ* Ar-ion sputtering before the top contact evaporation. The highest achieved values of $I_C R_{\mathrm{N}}$ at 4.2 K were $\sim$80-220 μV, the same order of magnitude as several previous studied NbN/TaN/NbN Josephson junction devices [23, 26], but less than optimal results $\sim$1-3 mV in Ref. [23]. For further increment of $I_C R_{\mathrm{N}}$ values, the control of the TaN layer resistivity (in between the NbN layers) should be optimized. Moreover, it was shown that Likharev's theory for SNS junctions followed the measured data quite well, indicating that the simple proximity effect based model can be used as a design guide for NbN/TaN/NbN Josephson junctions.

In addition, thin films of NbN was also successfully employed to investigate the mechanism of the suppression of superconductivity in the influence of an applied magnetic field.

The main results presented in this thesis are merely the initial steps of the vast

potential of pulsed laser deposited NbN based applications in the fields of NIS and SNS junctions. Also the very first steps for Cu/AlO_x-Al/Nb based devices were presented, and many interesting applications for example in thermometry and cooling are still to be developed with these Nb-based devices.

Bibliography

[1] POBELL, F., *Matter and Methods at Low Temperatures – Third, Revised and Expanded Edition* (Springe-Verlag, Berlin, 2007).

[2] TINKHAM, M., *Introduction to Superconductivity – 2nd ed.* (McGraw-Hill, New York, 1996).

[3] IBACH, H. AND LÜTH, H., *Solid-State Physics – An Introduction to Principles of Materials Science, Fourth Edition* (Springer-Verlag, Berlin, 2009).

[4] KOPPINEN, P. J., KÜHN, T., AND MAASILTA, I. J., *Effects of charging energy on sinis tunnel junction thermometry*. J. Low Temp. Phys. **154** (2009) 179 – 189.

[5] GIAZOTTO, F., HEIKKILÄ, T. T., LUUKANEN, A., SAVIN, A. M., AND PEKOLA, J. P., *Opportunities for mesoscopics in thermometry and refrigeration: Physics and applications*. Rev. Mod. Phys. **78** (2006) 217 – 274.

[6] KOPPINEN, P. J. AND MAASILTA, I. J., *Phonon cooling of nanomechanical beams with tunnel junctions*. Phys. Rev. Lett. **102** (2009) 165502.

[7] CLARK, A. M., MILLER, N. A., WILLIAMS, A., RUGGIERO, S. T., HILTON, G. C., VALE, L. R., BEALL, J. A., IRWIN, K. D., AND ULLOM, J. N., *Cooling of bulk material by electron-tunneling refrigerators*. Applied Physics Letters **86** (2005) 173508.

[8] MAISI, V. F., SAIRA, O.-P., PASHKIN, Y. A., TSAI, J. S., AVERIN, D. V., AND PEKOLA, J. P., *Real-time observation of discrete andreev tunneling events*. Phys. Rev. Lett. **106** (2011) 217003.

[9] KIM, N., HANSEN, K., TOPPARI, J., SUPPULA, T., AND PEKOLA, J., *Fabrication of mesoscopic superconducting Nb wires using conventional electron-beam lithographic techniques*. J. Vac. Sci. Technol. B **20** (2002) 386.

[10] TOPPARI, J. J., KÜHN, T., HALVARI, A. P., AND PARAOANU, G. S., *Method for finding the critical temperature of the island in a set structure*. Journal of Physics: Conference Series **150** (2009) 022088.

[11] LUUKANEN, A. AND PEKOLA, J. P., *A superconducting antenna-coupled hot-spot microbolometer*. Applied Physics Letters **82** (2003) 3970 – 3972.

[12] LUUKANEN, A., GROSSMAN, E. N., MILLER, A. J., HELISTÖ, P., PENTTILÄ, J., SIPOLA, H., AND SEPPÄ, H., *An ultra-low noise superconducting antenna-coupled microbolometer with a room-temperature read-out*. IEEE Microwave and Wireless Components Letters **16** (2006) 464 – 466.

[13] DOLATA, R., SCHERER, H., ZORIN, A. B., AND NIEMEYER, J., *Single electron transistors with Nb/AlO_x/Nb junctions*. Journal of Vacuum Science & Technology B: Microelectronics and Nanometer Structures **21** (2003) 775 – 780.

[14] HALBRITTER, J., *On the oxidation and on the superconductivity of niobium*. Applied Physics A: Materials Science & Processing **43** (1987) 1 – 28.

[15] SIMON, W., LIEBEMANN, E. K., SIMON, M., AND BUCHER, E., *Nb-Al-AlO_x-Al-Nb tunnel junctions using electron beam evaporation*. Journal of Applied Physics **72** (1992) 4474 – 4476.

[16] GURVITCH, M., WASHINGTON, M. A., AND HUGGINS, H. A., *High quality refractory josephson tunnel junctions utilizing thin aluminum layers*. Applied Physics Letters **42** (1983) 472 – 474.

[17] DUBOS, P., CHARLAT, P., CROZES, T., PANIEZ, P., AND PANNETIER, B., *Thermostable trilayer resist for niobium lift-off*. Journal of Vacuum Science & Technology B: Microelectronics and Nanometer Structures **18** (2000) 122 – 126.

[18] HOSS, T., STRUNK, C., AND SCHÖNENBERGER, C., *Nonorganic evaporation mask for superconducting nanodevices*. Microelectronic Engineering **46** (1999) 149 – 152.

[19] PEKOLA, J., KYYNÄRÄINEN, J., LEIVO, M., AND MANNINEN, A., *NIS chip refrigeration*. Cryogenics **39** (1999) 653 – 657.

[20] HALKOSAARI, J., *Niobipohjaiset SINIS-tunneliliitokset ja niiden käyttö lämpömittareina*, Master's thesis, University of Jyväskylä, Jyväskylä (2010).

[21] OYA, G.-I. AND ONODERA, Y., *Transition temperatures and crystal structures of single-crystal and polycrystalline NbN_x films*. Journal of Applied Physics **45** (1974) 1389 – 1397.

[22] TREECE, R. E., OSOFSKY, M. S., SKELTON, E. F., QADRI, S. B., HORWITZ, J. S., AND CHRISEY, D. B., *New phase of superconducting NbN stabilized by heteroepitaxial film growth*. Phys. Rev. B **51** (1995) 9356 – 9359.

[23] SETZU, R., BAGGETTA, E., AND VILLÉGIER, J. C., *Study of NbN Josephson junctions with a tantalum nitride barrier tuned to the metal-insulator transition*. Journal of Physics: Conference Series **97** (2008) 012077.

[24] KAWAKAMI, A., WANG, Z., AND MIKI, S., *Fabrication and characterization of epitaxial NbN/MgO/NbN Josephson tunnel junctions*. Journal of Applied Physics **90** (2001) 4796 – 4799.

[25] HELISTÖ, P., PENTTILÄ, J. S., SIPOLA, H., GRÖNBERG, L., MAIBAUM, F., LUUKANEN, A., AND SEPPÄ, H., *NbN vacuum bridge bolometer arrays with room temperature readout approaching photon noise limited THz imaging applications*. IEEE Transactions on Applied Superconductivity **17** (2007) 310 – 313.

[26] KAUL, A. B., WHITELEY, S. R., VAN DUZER, T., YU, L., NEWMAN, N., AND ROWELL, J. M., *Internally shunted sputtered NbN Josephson junctions with a TaNx barrier for nonlatching logic applications*. Applied Physics Letters **78** (2001) 99 – 101.

[27] LIKHAREV, K. K. AND SEMENOV, V. K., *RSFQ logic/memory family: a new Josephson-junction technology for sub-terahertz-clock-frequency digital systems*. IEEE Transactions on Applied Superconductivity **1** (1991) 3 – 28.

[28] KOBLISCHKA, M. R. AND WIJNGAARDEN, R. J., *Magneto-optical investigations of superconductors*. Superconductor Science and Technology **8** (1995) 199.

[29] LIKHAREV, K. K., *Superconducting weak links*. Rev. Mod. Phys. **51** (1979) 101 – 159.

[30] GIAEVER, I., *Energy gap in superconductors measured by electron tunneling*. Phys. Rev. Lett. **5** (1960) 147 – 148.

[31] CHAUDHURI, S. AND MAASILTA, I. J., *Cooling, conductance, and thermometric performance of nonideal normal metal-superconductor tunnel junction pairs*. Phys. Rev. B **85** (2012) 014519.

[32] VAN DUZER, T. AND TURNER, C. W., *Principles of Superconductive Devices and Circuits – Second Edition* (Upper Saddle River, New Jersey, 1999).

[33] COURT, N. A., FERGUSON, A. J., AND CLARK, R. G., *Energy gap measurement of nanostructured aluminium thin films for single cooper-pair devices*. Superconductor Science and Technology **21** (2008) 015013.

[34] MESERVEY, R. AND TEDROW, P. M., *Properties of very thin aluminum films*. Journal of Applied Physics **42** (1971) 51 – 53.

[35] KANG, L., JIN, B. B., LIU, X. Y., JIA, X. Q., CHEN, J., JI, Z. M., XU, W. W., WU, P. H., MI, S. B., PIMENOV, A., WU, Y. J., AND WANG, B. G., *Suppression of superconductivity in epitaxial NbN ultrathin films*. Journal of Applied Physics **109** (2011) 033908.

[36] KAMLAPURE, A., MONDAL, M., CHAND, M., MISHRA, A., JESUDASAN, J., BAGWE, V., BENFATTO, L., TRIPATHI, V., AND RAYCHAUDHURI, P., *Measurement of magnetic penetration depth and superconducting energy gap in very thin epitaxial NbN films*. Applied Physics Letters **96** (2010) 072509.

[37] WANG, Z., KAWAKAMI, A., UZAWA, Y., AND KOMIYAMA, B., *Superconducting properties and crystal structures of single-crystal niobium nitride thin films deposited at ambient substrate temperature*. Journal of Applied Physics **79** (1996) 7837 – 7842.

[38] SENAPATI, K., PANDEY, N. K., NAGAR, R., AND BUDHANI, R. C., *Normal-state transport and vortex dynamics in thin films of two structural polymorphs of superconducting NbN*. Phys. Rev. B **74** (2006) 104514.

[39] LEIVO, M., *On-chip cooling by quasiparticle tunnelling below 1 kelvin*, Ph.D. thesis, University of Jyväskylä, Jyväskylä (1999).

[40] DYNES, R. C., GARNO, J. P., HERTEL, G. B., AND ORLANDO, T. P., *Tunneling study of superconductivity near the metal-insulator transition*. Phys. Rev. Lett. **53** (1984) 2437 – 2440.

[41] PEKOLA, J. P., HEIKKILÄ, T. T., SAVIN, A. M., FLYKTMAN, J. T., GIAZOTTO, F., AND HEKKING, F. W. J., *Limitations in cooling electrons using normal-metal-superconductor tunnel junctions*. Phys. Rev. Lett. **92** (2004) 056804.

[42] PEKOLA, J. P., MAISI, V. F., KAFANOV, S., CHEKUROV, N., KEMPPINEN, A., PASHKIN, Y. A., SAIRA, O.-P., MÖTTÖNEN, M., AND TSAI, J. S., *Environment-assisted tunneling as an origin of the dynes density of states*. Phys. Rev. Lett. **105** (2010) 026803.

[43] O'NEIL, G. C., *Improving NIS Tunnel Junction Refrigerators: Modeling, Materials, and Traps*, Ph.D. thesis, University of Colorado, Boulder (2011).

[44] RAJAURIA, S., GANDIT, P., FOURNIER, T., HEKKING, F. W. J., PANNETIER, B., AND COURTOIS, H., *Andreev current-induced dissipation in a hybrid superconducting tunnel junction*. Phys. Rev. Lett. **100** (2008) 207002.

[45] JOSEPHSON, B. D., *Possible new effects in superconductive tunnelling*. Physics Letters **1** (1962) 251 – 253.

[46] FEYNMAN, R. P., LEIGHTON, R. B., AND SANDS, M., *The Feynman Lectures on Physics – The Definite Edition Volume III* (Addison Wesley, California, 2006).

[47] AMBEGAOKAR, V. AND BARATOFF, A., *Tunneling between superconductors*. Phys. Rev. Lett. **10** (1963) 486 – 489.

[48] DELIN, K. A. AND KLEINSASSER, A. W., *Stationary properties of high-critical-temperature proximity effect Josephson junctions*. Superconductor Science and Technology **9** (1996) 227.

[49] KITTEL, C., *Introduction to solid state physics – Seventh Edition* (John Wiley & Sons, New York, 1996).

[50] MCCUMBER, D. E., *Effect of ac impedance on dc voltage-current characteristics of superconductor weak-link junctions*. Journal of Applied Physics **39** (1968) 3113 – 3118.

[51] STEWART, W. C., *Current-voltage characteristics of Josephson junctions*. Applied Physics Letters **12** (1968) 277 – 280.

[52] HEIKKILÄ, T., *Superconducting Proximity Effect in Mesoscopic Metals*, Ph.D. thesis, Helsinki University of Technology, Espoo (2002).

[53] LÜTH, H., *Solid Surfaces, Interfaces and Thin Films – Fifth Edition* (Springer-Verlag, Berlin, 2010).

[54] KOSKI, J. V., PELTONEN, J. T., MESCHKE, M., AND PEKOLA, J. P., *Laterally proximized aluminum tunnel junctions*. Applied Physics Letters **98** (2011) 203501.

[55] DE GENNES, P. G., *Boundary effects in superconductors*. Rev. Mod. Phys. **36** (1964) 225 – 237.

[56] LIKHAREV, K. K., MUKHANOV, O. A., AND SEMENOV, V. K., *Resistive single flux quantum logic for the Josephson-junction digital technology, SQUID '85 – Superconducting Quantum Interference Devices and their Applications* (Walter de Gruyter & Co., Berlin, 1985).

[57] CHEN, W., RYLYAKOV, A. V., PATEL, V., LUKENS, J. E., AND LIKHAREV, K. K., *Superconductor digital frequency divider operating up to 750 GHz*. Applied Physics Letters **73** (1998) 2817 – 2819.

[58] CHEN, W., RYLYAKOV, A., PATEL, V., LUKENS, J., AND LIKHAREV, K., *Rapid single flux quantum T-flip flop operating up to 770 GHz*. IEEE Transactions on Applied Superconductivity **9** (1999) 3212 – 3215.

[59] KAPLUNENKO, V. K., *Fluxon interaction in an overdamped Josephson transmission line*. Applied Physics Letters **66** (1995) 3365 – 3367.

[60] ROWELL, J. M. AND TSUI, D. C., *Hot electron temperature in InAs measured by tunneling*. Phys. Rev. B **14** (1976) 2456 – 2463.

[61] KARVONEN, J. T. AND MAASILTA, I. J., *Influence of phonon dimensionality on electron energy relaxation*. Phys. Rev. Lett. **99** (2007) 145503.

[62] KARVONEN, J., TASKINEN, L., AND MAASILTA, I., *Influence of temperature gradients on tunnel junction thermometry below 1 k: Cooling and electron-phonon coupling*. Journal of Low Temperature Physics **149** (2007) 121 – 135.

[63] LEIVO, M. M., PEKOLA, J. P., AND AVERIN, D. V., *Efficient Peltier refrigeration by a pair of normal metal/insulator/superconductor junctions*. Applied Physics Letters **68** (1996) 1996 – 1998.

[64] NAHUM, M. AND MARTINIS, J. M., *Ultrasensitive-hot-electron microbolometer*. Applied Physics Letters **63** (1993) 3075 – 3077.

[65] NAHUM, M., EILES, T. M., AND MARTINIS, J. M., *Electronic microrefrigerator based on a normal-insulator-superconductor tunnel junction*. Applied Physics Letters **65** (1994) 3123 – 3125.

[66] MANNINEN, A. J., LEIVO, M. M., AND PEKOLA, J. P., *Refrigeration of a dielectric membrane by superconductor/insulator/normal-metal/insulator/superconductor tunneling*. Applied Physics Letters **70** (1997) 1885 – 1887.

[67] RAJAURIA, S., LUO, P. S., FOURNIER, T., HEKKING, F. W. J., COURTOIS, H., AND PANNETIER, B., *Electron and phonon cooling in a superconductor–normal-metal–superconductor tunnel junction*. Phys. Rev. Lett. **99** (2007) 047004.

[68] MILLER, N. A., O'NEIL, G. C., BEALL, J. A., HILTON, G. C., IRWIN, K. D., SCHMIDT, D. R., VALE, L. R., AND ULLOM, J. N., *High resolution x-ray transition-edge sensor cooled by tunnel junction refrigerators*. Applied Physics Letters **92** (2008) 163501.

[69] PEKOLA, J. P., ANGHEL, D. V., SUPPULA, T. I., SUOKNUUTI, J. K., MANNINEN, A. J., AND MANNINEN, M., *Trapping of quasiparticles of a nonequilibrium superconductor*. Applied Physics Letters **76** (2000) 2782 – 2784.

[70] WELLSTOOD, F. C., URBINA, C., AND CLARKE, J., *Hot-electron effects in metals*. Phys. Rev. B **49** (1994) 5942 – 5955.

[71] CHRISEY, D. G. AND HUBLER, G. K. (eds.), *Pulsed Laser Deposition of Thin Films* (John Wiley & Sons, New York, 1994).

[72] EASON, R. (ed.), *Pulsed Laser Deposition of Thin Films, Applications – Led Growth of Fundamental materials* (2007).

[73] LOWNDES, D. H., GEOHEGAN, D. B., PURETZKY, A. A., NORTON, D. P., AND ROULEAU, C. M., *Synthesis of novel thin-film materials by pulsed laser deposition*. Science **273** (1996) 898 – 903.

[74] LEE, L. P., CHAR, K., COLCLOUGH, M. S., AND ZAHARCHUK, G., *Monolithic 77 k dc SQUID magnetometer*. Applied Physics Letters **59** (1991) 3051 – 3053.

[75] LI, Q., XI, X. X., WU, X. D., INAM, A., VADLAMANNATI, S., MCLEAN, W. L., VENKATESAN, T., RAMESH, R., HWANG, D. M., MARTINEZ, J. A., AND NAZAR, L., *Interlayer coupling effect in high-T_C superconductors probed by $YBa_2Cu_3O_{7-x}$/$PrBa_2Cu_3O_{7-x}$ superlattices*. Phys. Rev. Lett. **64** (1990) 3086 – 3089.

[76] LEE, S. K. AND SON, J. Y., *Epitaxial growth of thin films and nanodots of ZnO on Si(111) by pulsed laser deposition*. Applied Physics Letters **100** (2012) 132109.

[77] HAKOLA, A., *Thin-Film Deposition Using Laser Ablation: Application to Ferromagnetic Shape-Memory Materials and Methods for Spatial Shaping of Laser Beams*, Ph.D. thesis, Helsinki University of Technology, Espoo (2006).

[78] CHICHKOV, B. N., MOMMA, C., NOLTE, S., VON ALVENSLEBEN, F., AND TÜNNERMANN, A., *Femtosecond, picosecond and nanosecond laser ablation of solids*. Applied Physics A: Materials Science & Processing **63** (1996) 109 – 115.

[79] LUNNEY, J. G. AND JORDAN, R., *Pulsed laser ablation of metals*. Applied Surface Science **127** (1998) 941 – 946.

[80] WILLMOTT, P. R. AND HUBER, J. R., *Pulsed laser vaporization and deposition*. Rev. Mod. Phys. **72** (2000) 315 – 328.

[81] SINGH, R. K. AND NARAYAN, J., *Pulsed-laser evaporation technique for deposition of thin films: Physics and theoretical model*. Phys. Rev. B **41** (1990) 8843 – 8859.

[82] BOSE, S. K., *Spin Polarized Transport in Selfassembled Fe Nano-Plaquettes and Distributed NbN-Fe-NbN Josephson Junction Arrays*, Ph.D. thesis, Department of Physics Indian Institute of Technology, Kanpur (2010).

[83] CHAUDHURI, S., *Studies of the co-existing phases and photo-induced insulator-metal transition in charge-ordered manganites*, Ph.D. thesis, Department of Physics Indian Institute of Technology, Kanpur (2008).

[84] ZHANG, Z. AND LAGALLY, M. G., *Atomistic processes in the early stages of thin-film growth*. Science **276** (1997) 377 – 383.

[85] VENABLES, J. A., SPILLER, G. D. T., AND HANBUCKEN, M., *Nucleation and growth of thin films*. Reports on Progress in Physics **47** (1984) 399.

[86] FRANCHY, R., *Growth of thin, crystalline oxide, nitride and oxynitride films on metal and metal alloy surfaces*. Surface Science Reports **38** (2000) 195 – 294.

[87] CLELAND, A. N., *Foundations of Nanomechanics, From Solid-State Theory to Device Applications* (Springer-Verlag, Berlin, 2003).

[88] PIERSON, H. O., *Handbook of Chemical Vapor Deposition (CVD), Principles, Technology, and Applications – Second Edition* (William Andrew Publishing, New York, 1999).

[89] LINDELL, A., *Nanofabrication by atomic force microscopy, electron beam lithography and reactive ion etching*, Ph.D. thesis, University of Jyväskylä, Jyväskylä (2000).

[90] FRANSSILA, S., *Introduction to Microfabrication – Second Edition* (John Wiley & Sons, Chichester, 2010).

[91] HU, W., SARVESWARAN, K., LIEBERMAN, M., AND BERNSTEIN, G. H., *Sub-10 nm electron beam lithography using cold development of poly(methylmethacrylate)*. Journal of Vacuum Science & Technology B: Microelectronics and Nanometer Structures **22** (2004) 1711 – 1716.

[92] KARVONEN, J., *Thermal properties in low dimensional structures below 1 K*, Ph.D. thesis, University of Jyväskylä, Jyväskylä (2009).

[93] BHUSHAN, B. (ed.), *Springer Handbook of Nanotechnology* (Springer-Verlag, Berlin, 2004).

[94] BEHRISCH, R. (ed.), *Sputtering by Particle Bombardment 1 – Physical Sputtering of Single-Element Solid* (Springe-Verlag, Berlin, 1981).

[95] CUKAUSKAS, E. J., CARTER, W. L., AND QADRI, S. B., *Superconducting and structure properties of niobium nitride prepared by rf magnetron sputtering*. Journal of Applied Physics **57** (1985) 2538 – 2542.

[96] PEKOLA, J. P. AND KAUPPINEN, J. P., *Insertable dilution refrigerator for characterization of mesoscopic samples*. Cryogenics **34** (1994) 843 – 845.

[97] ZORIN, A. B., *The thermocoax cable as the microwave frequency filter for single electron circuits*. Review of Scientific Instruments **66** (1995) 4296 – 4300.

[98] KING, R. B. (ed.), *Encyclopedia of Inorganic Chemistry - Volume 5* (John Wiley & Sons, Chichester, 1995).

[99] HAVEY, K., ZABINSKI, J., AND WALCK, S., *The chemistry, structure, and resulting wear properties of magnetron-sputtered NbN thin films*. Thin Solid Films **303** (1997) 238 – 245.

[100] WANG, Z., TERAI, H., KAWAKAMI, A., AND UZAWA, Y., *Interface and tunneling barrier heights of NbN/AlN/NbN tunnel junctions*. Applied Physics Letters **75** (1999) 701 – 703.

[101] HAJENIUS, M., BASELMANS, J. J. A., GAO, J. R., KLAPWIJK, T. M., DE KORTE, P. A. J., VORONOV, B., AND GOL'TSMAN, G., *Low noise NbN superconducting hot electron bolometer mixers at 1.9 and 2.5 THz*. Superconductor Science and Technology (2004) S224.

[102] MARSILI, F., BITAULD, D., FIORE, A., GAGGERO, A., MATTIOLI, F., LEONI, R., BENKAHOUL, M., AND LÉVY, F., *High efficiency NbN nanowire superconducting single photon detectors fabricated on MgO substrates from a low temperature process*. Optics Express **16** (2008) 3191 – 3196.

[103] LENGAUER, W., BOHN, M., WOLLEIN, B., AND LISAK, K., *Phase reactions in the Nb-N system below 1400 °C*. Acta Materialia **48** (2000) 2633 – 2638.

[104] TREECE, R. E., HORWITZ, J. S., CHRISEY, D. B., DONOVAN, E. P., AND QADRI, S. B., *Pulsed laser ablation synthesis of NbN_x ($0 \leq x \leq 1.3$) thin films*. Chem. Mater. **6** (1994) 2205 – 2207.

[105] OHASHI, Y., MOTOHASHI, T., MASUBUCHI, Y., AND KIKKAWA, S., *Crystal structure and superconductive characteristics of $Nb_{0.89}Al_{0.11}$ oxynitrides*. Journal of Solid State Chemistry **183** (2010) 1710 – 1714.

[106] MARTIENSSEN, W. AND WARLIMONT, H. (eds.), *Springer Handbook of Condensed Matter and Materials Data* (Springer, Berlin, 2005).

[107] OYA, G.-I. AND ONODERA, Y., *Superconducting transition temperatures of vapor-deposited niobium nitride*. Journal of Vacuum Science and Technology **7** (1970) S44 – S47.

[108] GOTOH, Y., TSUJI, H., AND ISHIKAWA, J., *Application of compact microwave ion source to low temperature growth of transition metal nitride thin films for vacuum microelectronics devices*. Review of Scientific Instruments **71** (2000) 1002 – 1005.

[109] BOFFA, V., GAMBARDELLA, U., MAROTTA, V., MORONE, A., MURTAS, F., ORLANDO, S., AND PARISI, G., *NbN superconducting thin films grown by pulsed laser ablation*. Applied Surface Science **106** (1996) 361 – 364.

[110] OYA, G.-I. AND ONODERA, Y., *Phase transformations in nearly stoichiometric NbN_x*. Journal of Applied Physics **47** (1976) 2833 – 2840.

[111] HALBRITTER, J. AND DARLINSKI, A., *Angle resolved XPS studies of oxides at Nb-, NbN-, NbC- and Nb_3Sn-surfaces*. IEEE Transactions on Magnetics **23** (1987) 1381 – 1384.

[112] DARLINSKI, A. AND HALBRITTER, J., *Angle-resolved XPS studies of oxides at NbN, NbC and Nb surfaces*. Surface and Interface Analysis **10** (1987) 223 – 237.

[113] GANIN, A. Y., KIENLE, L., AND VAJENINE, G. V., *Plasma-enhanced CVD synthesis and structural characterization of Ta_2N_3*. European Journal of Inorganic Chemistry **16** (2004) 3233 – 3239.

[114] ROSSNAGEL, S. M. AND KIM, H., *Diffusion barrier properties of very thin TaN with high nitrogen concentration*. Journal of Vacuum Science & Technology B: Microelectronics and Nanometer Structures **21** (2003) 2550 – 2554.

[115] KILBANE, F. M. AND HABIG, P. S., *Superconducting transition temperatures of reactively sputtered films of tantalum nitride and tungsten nitride*. Journal of Vacuum Science and Technology **12** (1975) 107 – 109.

[116] BHAT, A., MENG, X., WONG, A., AND VAN DUZER, T., *Superconducting NbN films grown using pulsed laser deposition for potential application in internally shunted Josephson junctions*. Superconductor Science and Technology **12** (1999) 1030.

[117] RADPARVAR, M., BERRY, M., DRAKE, R., FARIS, S., WHITELEY, S., AND YU, L., *Fabrication and performance of all NbN Josephson junction circuits*. IEEE Transactions on Magnetics, **23** (1987) 1480 – 1483.

[118] KAUL, A. AND VAN DUZER, T., *NbN/TaNx/NbN SNS Josephson junctions by pulsed laser deposition*. IEEE Transactions on Applied Superconductivity, **11** (2001) 88 – 91.

[119] YU, L., GANDIKOTA, R., SINGH, R. K., GU, L., SMITH, D. J., MENG, X., ZENG, X., VAN DUZER, T., ROWELL, J. M., AND NEWMAN, N., *Internally shunted Josephson junctions with barriers tuned near the metal-insulator transition for RSFQ logic applications*. Superconductor Science and Technology (2006) 719.

[120] BOSE, S., RAYCHAUDHURI, P., BANERJEE, R., VASA, P., AND AYYUB, P., *Mechanism of the size dependence of the superconducting transition of nanostructured Nb*. Phys. Rev. Lett. **95** (2005) 147003.

[121] PARK, S. I. AND GEBALLE, T. H., *Superconducting tunneling in ultrathin Nb films*. Phys. Rev. Lett. **57** (1986) 901 – 904.

[122] FERGUSON, A. J., ANDRESEN, S. E., BRENNER, R., AND CLARK, R. G., *Spin-dependent quasiparticle transport in aluminum single-electron transistors*. Phys. Rev. Lett. **97** (2006) 086602.

[123] TOWNSEND, P., GREGORY, S., AND TAYLOR, R. G., *Superconducting behavior of thin films and small particles of aluminum*. Phys. Rev. B **5** (1972) 54 – 66.

[124] CHOCKALINGAM, S. P., CHAND, M., KAMLAPURE, A., JESUDASAN, J., MISHRA, A., TRIPATHI, V., AND RAYCHAUDHURI, P., *Tunneling studies in a homogeneously disordered s-wave superconductor: NbN*. Phys. Rev. B **79** (2009) 094509.

[125] VAN DOVER, R. B., BACON, D. D., AND SINCLAIR, W. R., *Superconductive tunneling into NbN deposited near room temperature*. Applied Physics Letters **41** (1982) 764 – 766.

[126] VECHTEN, D. V. AND LIEBMAN, J. F., *Considerations on the selection of artificial tunneling barriers*. Journal of Vacuum Science & Technology A: Vacuum, Surfaces, and Films **3** (1985) 1881 – 1883.

[127] SHOJI, A., AOYAGI, M., KOSAKA, S., SHINOKI, F., AND HAYAKAWA, H., *Niobium nitride Josephson tunnel junctions with magnesium oxide barriers*. Applied Physics Letters **46** (1985) 1098 – 1100.

[128] HATANO, M., NISHINO, T., AND KAWABE, U., *Effects of thermal annealing on superconducting Nb and NbN films*. Journal of Vacuum Science and Technology A: Vacuum, Surfaces, and Films **6** (1988) 2381 – 2385.

[129] KIRTLEY, J. R., RAIDER, S. I., FEENSTRA, R. M., AND FEIN, A. P., *Spatial variation of the observed energy gap in granular superconducting NbN films*. Applied Physics Letters **50** (1987) 1607 – 1609.

[130] YU, L., STAMPFL, C., MARSHALL, D., ESHRICH, T., NARAYANAN, V., ROWELL, J. M., NEWMAN, N., AND FREEMAN, A. J., *Mechanism and control of the metal-to-insulator transition in rocksalt tantalum nitride*. Phys. Rev. B **65** (2002) 245110.

[131] TABORYSKI, R., KUTCHINSKY, J., RN BINDSLEV HANSEN, J., WILDT, M., RENSEN, C. B. S., AND LINDELOF, P. E., *Multiple Andreev reflections in diffusive SNS structures*. Superlattices and Microstructures **25** (1999) 829 – 837.